Study of particle control based on Hα line measurement and Monte-Carlo simulation in the GAMMA 10 tandem mirror

Katsuhiro HOSOI

February 2014

Study of particle control based on Hα line measurement and Monte-Carlo simulation in the GAMMA 10 tandem mirror

Katsuhiro HOSOI
Doctoral Program in Physics

Submitted to the Graduate School of
Pure and Applied Sciences
in Partial Fulfillment of the Requirements
for the Degree of Doctor of Philosophy in
Science

at the
University of Tsukuba

Contents

Chapter 1 Introduction

In the plasma confinement devices, particle control is a very important issue in order to obtain the high performance plasma. According to the good confinement for high performance plasma, the control of the plasma particle and particle source has a crucial role in order to maintain of the proper particle balance. In addition, control of the neutral particle in the peripheral region is very important in order to obtain the high performance plasma. As an index of the efficiency of particle supply, reduction of the neutral particle in the peripheral region is an important issue. It has been reported that neutral particles in the boundary region have a sufficient influence on the plasma condition in a core region and transition phenomena of the plasma confinement mode [1, 2]. We get closer to the time of starting the ITER operation. However there are some unexplained physics phenomena in detail related to the neutral particles. For example, recycling phenomena in peripheral region of plasma affected to the confinement of the core plasma. A number of Experiments have been performed in some experimental devices under the bi-directional collaboration as taking advantage of the device's features. GAMMA 10 is the tandem mirror type linear device. Utilizing the simple magnetic line configuration and multitude of observation port, we could measure the plasma parameters under the simplified condition of physics phenomena. It is the suitable for understanding the basic physics.

GAMMA 10 at the University of Tsukuba is an axi-symmetrized tandem mirror device with thermal barrier [3-6]. GAMMA 10 consists of a central-cell, anchor-cells, plug/barrier-cells and end-cells. In GAMMA 10, plasma boundary has been determined by a fixed type and two movable type of limiters. The GAMMA 10 plasma is heated and maintained by ion cyclotron rang frequency (ICRF) waves [4]. Therefore, a significant difference occurs between the ion temperature and the electron temperature in the plasma. Electron cyclotron resonance heating (ECRH) is injected in order to improve the plasma parameter and prevent the electron drag caused by this temperature difference. However the decrease of the stored energy is occasionally observed in the ECRH period [7]. It is speculated that the decrease of the stored energy is caused by the particle loss. From a viewpoint of the particle balance, total particle source was investigated in the whole of central cell in order to optimize the ECRH injection. Evaluation of ionization rate of the neutral particles enables us to obtain the information on the plasma confinement, since the neutral particles are the origin of the plasma particles.

For the neutral particle source in the plasma confinement devices, a gas puffer and a pellet injection are widely applied [8]. Fuel gas is injected into the vacuum vessel and supplied to the edge plasma. Pellet injection is also used for particle sources in the core region of the plasma in order to obtain the high density plasma [9]. The significant feature of the pellet injection is that the injected object is solid hydrogen. A solid hydrogen pellet is accelerated by compressed gas or centrifugal force and injected into plasma with several hundred meter/sec. In addition to the above external

factors, recycling phenomena on the vacuum vessel and interior components such as antenna of ICRF play an important role on the large amount of neutral source [10-14]. It is difficult to control such recycling particles because the recycling particles are passively given according to the condition of the wall, the plasma parameter. The recycling particle is able to be controlled partially by changing the limiter diameter only in the case of the movable type limiters.

Neutral particle form conventional gas puffer could not injected deeper into the core plasma in the high performance devices. Supersonic Molecular Beam Injection (SMBI), which was developed by L.Yao et al. [15], constitutes a new method of gas fueling. SMBI provides high-speed and high-directive gas injection by using a plenum pressure higher than what is used in conventional gas puffing. SMBI was newly installed at the central-cell of GAMMA 10 [16]. SMBI experiment was supported by the bi-directional collaboration research program of Kyoto University [17, 18, 58]. High speed camera also has been installed. The visible emission intensity from the plasma was captured in order to investigate the neutral particle and the plasma behavior [19]. Based on the both results of the experiments and the simulations, the difference between the conventional gas puffer and SMBI is clarified, and the mechanism of particle supply is investigated by using a new particle supply method, SMBI.

For the clarification of the neutral transport, the coupling analysis with the experimental approach and the numerical approach by using a simulation code such as a Monte-Carlo method have been developed [20-25]. On measurements of the neutral particles, Balmer-line emission from hydrogen isotopes has been commonly measured in order to estimate the local neutral behavior. An Hα line emission detector with a photo multiplier tube and an interference filter is commonly utilized for the plasma diagnostic. As well as Hα line emission detector, high-speed camera is a powerful measurement tool. A two-dimentional image can be captured by High-speed camera, and the image makes it possible to obtain an instant understanding for the plasma position and neutral particle behavior in the peripheral region. In addition, measurement of 2-dimentional image is suitable for investigating the behavior of neutral particle from local particle supply such as SMBI. Furthermore, by using inference filter, the specific wave length among the visible light range can be selected.

In the GAMMA 10 tandem mirror, Hα line emission detectors are located in vacuum vessel along the magnetic field obtaining the axial structure of neutral particle density [26, 27], and furthermore, high-speed camera has been applied in the central mid-plane. By using the dual blanch optical fiber bundles, the camera system has a line of sight in the horizontal direction and one in the vertical direction of the plasma cross-section. This measurement system enables us to obtain the local information of the neutral particles. In addition, the Monte-Carlo simulation has been developed for the analysis of the more detail neutral transport. The DEGAS code is a simulation code which simulates the neutral transport [28, 29]. In this code, Monte-Carlo method is used for the particle tracking analysis. The version 35 of DEGAS code (DEGAS35) was firstly adapted for neutral transport simulation in the central cell [10]. The meshes for this code are constructed as a 2-dimensional axis. Mesh configurations and plasma parameters in the cell of simulation space are

assumed to be axi-symmetric. However the DEGAS code has been developed for the simulation of the high plasma density region such as tokamak plasmas. Therefore it was reported that the density profile of neutral hydrogen atoms calculated by the DEGAS code was significantly different from the experimental results in the case that the plasma density was less than $10^{19}m^{-3}$[30]. This discrepancy was attributable to the production of hydrogen atoms at excited levels by the direct-dissociation of hydrogen molecules upon electron impact. The effect of dissociative-excitation reactions of neutral hydrogen molecules are additionally included so as to calculate low density plasma in the plasma edge region for applying the DEGAS code to the GAMMA 10 plasma [10, 22]. In order to investigate the neutral transport due to the non-axisymmetric structure of the wall geometry and plasma parameter, and the non-uniform distribution of the neutral sources, the version 63 of DEGAS code (DEGAS63) was successfully utilized [10,22,25,31-37]. The DEGAS code has been applied in 3-D simulation of neutral transport in a part of central-cell and anchor-cell. 3-D simulation mesh model are expanded in order to evaluate the amount of the generated particles in the central cell. Finally, the fully 3-dimentional mesh model in a whole area of central cell and a part of anchor cell is accomplished.

In this model, interior components such as the limiters and antennas for ICRF heating are included in the detailed structure. SMBI injection port and a nozzle for SMBI are newly installed in this mesh model. By the numerical simulation of the neutral particles, the neutral densities are determined in the whole 3-dimensional meshes. Based on the neutral density, Hα emission in the each mesh is calculated on the basis of a collisional-radiative model (CR-model). The calculated Hα emission is compared with calibrated measurement results by the Hα line detectors and the high-speed camera. This coupling method is quite useful for analyzing the complicated neutral behavior.

The purpose of this thesis is to measure the spatial neutral particle behavior under the different experimental conditions and the different particle sources by axially aligned Hα detectors and high-speed camera, in the liner device which has many observation ports. Furthermore we clarify the neutral particle behavior which is independent of the configuration of the devices, of the particle sources and of the experimental conditions, by reproducing the experimental results with the fully 3-dimentional neutral transport simulation code (DEGAS). These results enable us to contribute the study of neutral particle for the complicated devices such as helical type devices, or tokamak devices as represented by ITER.

Outline of the thesis is as follows. After introducing the first chapter, chapter 2 describes the feature of GAMMA 10 with the schematic views. Heating system, pumping system, fueling system, and diagnostic systems is also described. In chapter 3, the analysis method for neutral transport is explained in detail. The measurement principle of Hα emission is mentioned. The analysis method by using CR-model and Monte-Carlo simulation method are explained. In chapter 4, the mechanism of degradation of the plasma parameters in C-ECRH experiments is described. Total generated particle in the central cell is evaluated by using the neutral transport simulation for optimization of the C-ECRH experiments. In chapter 5, characteristic of SMBI which is new particle supply method

is discussed based on 2-dimentional image captured by high-speed camera. In addition, the neutral particle behavior is investigated by using Monte-Carlo simulation code (DEGAS). In simulation results, the spatial distribution of neutral particle behavior on the plasma cross-section is discussed. Finally, this thesis is concluded in chapter 6.

Chapter 2 Experimental setup

2.1 GAMMA 10

The GAMMA 10 tandem mirror is open magnetic plasma-confining device with thermal barrier [3]. It consists of central-cell, anchor-cells, plug/barrier-cells, and end-cells. Mid-plane of the central-cell is z = 0 cm and west and east sides correspond to plus and minus in z-axis, respectively. We also take the vertical and horizontal direction as x and y axes with these origins at the machine axis. Central-cell is the main region to confine plasma and 6 m in length and the diameter of 1 m. In the standard operation, the magnetic strength in central mid-plane is 0.405 T and the mirror ratio of the central-cell is 5. Mirror-throat regions which exist between the central-cell and each anchor-cell have the first mirror with strong magnetic field for the confining plasma in the central-cell. The anchor-cells are connected to the central-cell via both mirror throat regions. The anchor-cell has non-axisymmetric magnetic structure with minimum-B configuration for the MHD stability. The plug/barrier cells are located at the outside of both anchor-cells. Plug potential, which is produced with electron cyclotron heating, confines the plasma from the central- and anchor-cell. In the central cell and plug/barrier cells, the axisymmetric mirror magnetic field is produced by circular coils. The minimum-B field in the anchor cell is produced by the main base ball coil which is bounded two trace-coils and two base-ball coils for re-circularization of the magnetic flux tube. Figure 2.1 shows the schematic view of the GAMMA 10 tandem mirror. The vacuum vessel, coil arrangement, magnetic field profile and the potential of the plasma is shown in Fig. 2.1. In standard hot-ion mode plasmas, initial plasma is build up by plasma guns located in both ends. Then plasma is sustained by gas puffing coupling with ion cyclotron heating. ECRH and neutral beam injection (NBI) are additionally supplied for the plasma production and heating.

2.2 Pumping System

There are three types of pumping systems in GAMMA 10, which are turbo-molecular pumps (TMP), helium cryosorption pump systems (CP), and liquid helium cryopanel (LHP) systems. TMPs are mounted in the central cell, the anchor cells, and the end cells. The TMP in the end cells and one of the central cell have the pumping speed of 15,00 l/s, the pumping speed of other TMP are 2,500 l/s. CPs are mounted in the central cell, end-mirror tanks, east barrio NBI tank, and the end cells. One in the central cell has the pumping speed of 10,000 l/s, and the others have 1,800 l/s for hydrogen gas. LHPs are located on the end-mirror tanks and on the anchor NBI tanks. The LHP consists of

stainless steel panels cooled to 3.5 K by the liquid helium. The pumping speeds located on the end-mirror tanks and on the anchor NBI tanks are 9.0×10^5 l/s, 4.0×10^5 l/s, respectively.

2.3 Plasma Gun

For starting up the plasma, two plasma guns using magneto-plasma-dynamic (MPD) jet are installed in both ends of GAMMA 10. The plasmas produced by these guns are injected into the central cell along the magnetic field lines by J×B force. The initial plasma produced by the plasma gun can build up the plasma in the central cell effectively with the gas puffing and heating systems. The pulse length of the arc plasma is usually 1 ms.

2.4 Fueling system

2.4.1 Conventional gas puffer

The conventional gas puff system has been used since early fusion plasma experiments. Fuel gas is injected into the vacuum vessel and supplied to the edge plasma. Piezo electric valves are often used in this system. This system has a drawback of low fueling efficiency. Especially in high performance plasma, most of the particles supplied by gas puffer are ionized in peripheral region of the plasma. Main gas puffer has been installed at the both of the central cell in GAMMA 10.

2.4.2 Pellet injector

The ice pellet injection system is considered as a favorable method to refuel magnetically confined plasma. Hydrogen gas is cooled by a refrigerator to ~10 K to create ice pellets. The advantage of this system is high fueling efficiency reaching 100 %. The density of the core plasma effectively can be increased by ice pellet injection. In the previous experiments, fueling by using pellet injection system was carried out in GAMMA 10 [38, 39]. This system consists of a pipe-gun type pneumatic pellet injector system made by the Oak Ridge National Laboratory and modified by Plasma Research Center of the University of Tsukuba [40]. The eight barrels are mounted into the injector and inner diameters of the barrels are 0.39, 0.58, 0.79 and 0.99. The pellet was injected from under the midplane of the central cell through the 6 m length of Teflon tube with the 1/4 inch inner diameter.

2.4.3 Supersonic molecular beam injector

Supersonic molecular beam injection (SMBI) system has been developed as a new fueling method that can combine both advantage of the conventional gas puffer and the pellet injection [15]. In this system, high pressure gas is injected by using fast solenoid valve. SMBI is considered especially effective for small and relatively low-density devices such as GAMMA 10 and has been installed at the mid-plane of the central cell [16]. SMBI provides high-speed and high-directive gas injection by using a plenum pressure higher than what is used in conventional gas puffing, so that neutral particles can be injected deeper into the core plasma.

2.5 Heating Systems

2.5.1 Ion Cyclotron Range of Frequency (ICRF) systems

ICRF systems are used in GAMMA 10 for the production and heating of the plasmas [41, 42]. Two kinds of ICRF antennas are installed in GAMMA 10 for the standard operation. These antennas are both end of the central cell. For the ion heating and plasma production, one is called RF1 system connected to the NAGOYA TYPE-III antenna, which excite ICRF fast waves (RF1; ~10MHz) for the plasma production and/or ion heating in the anchor cells. For the ion heating in the central cell, RF2 heating system is used with double-half-turn antenna by using ICRF slow waves (RF2; 6.36 MHz) which correspond to the ion cyclotron resonance frequency (ω_{ci}) near the central cell midplane.

2.5.2 Electron Cyclotron Resonance Heating (ECRH) systems

ECRH system has been installed in the GAMMA 10 tandem mirror device [43]. ECRH systems with four 28 GHz gyrotorons are applied to create the confining potentials in the plug/barrier cells. The axial-confining potentials for ion are formed by plug ECRH (P-ECRH) at a position where the magnetic field strength is 1 T. The heating point has a steep slope of the magnetic field. Barrier ECRH (B-ECRH) systems are used at the barrier midplane so as to form a negative potential relative to the central cell. The central cell ECRH (C-ECRH) system consists of a gyrotron with the frequency of 28 GHz. The aim of this system is the heating of the electron in the central cell in order to suppress the ion energy loss caused by electron drag.

2.5.3 Neutral Beam Injection (NBI) systems

Three NBI systems are used for the ion heating or sustaining the potential in the both barrier regions to produce sloshing ion (sloshing NBI). The sloshing ions contribute to the sustainment of the potential dip of thermal barrier. The NBI systems in the anchor cell are used for the fueling and heating and MHD stabilization by injecting 25 keV neutral hydrogen beams into the anchor cell midplane. The other NBI system is installed in the central cell for ion heating and fueling.

2.6 Diagnostics

2.6.1 Plasma pressure measurement

Diamagnetic loop are installed in the central cell to measure the central plasma pressure and anisotropy. Diamagnetic loop consists of the inner loop and the outer loop. The amount of diamagnetism is proportional to the product of the plasma density and temperature. The concentric loop can cancel the noise signal caused by the ripple of the magnetic field. In standard operation, it has been found that the ion temperature has been much higher than that of the electron.

2.6.2 Ion and electron temperature measurements

Radial profile of the ion temperature in the central cell midplane is measured by the charge-exchange neutral particle analyzer (CX-NPA). The power balance is investigated by using the results of the CX-NPA. Thomson scattering (TS) system is installed in the central cell for measuring the electron temperature [44]. TS system consists of laser, incident optics, light-collection optics, signal-detection electronics, and data recording system.

2.6.3 Plasma particle density measurements

The plasma line density is measured by micro wave interferometer systems. Microwave interferometers are installed in each cell of GAMMA 10 in order to measure the axial distribution of the line density. By using an Abel inversion technique with a radial scan measurement, the radial profile of the electron density at the central cell midplane can be determined. TS system is also used for measuring the electron density at the central cell.

2.6.4 Loss particle measurement

Ion sensitive probe (ISP) has been installed in the central cell [45]. ISP consists of the ion collector, electron guard electrode and secondary repeller electrode. By making use of the difference of the Larmor radius between ion and electron, ion current is selectively measured by ISP. In this thesis, ISP signal is an index of the radial loss particles. Loss electron diagnostics (LED) has been installed both end cells [46]. LED consists of collector, collector shield, secondary electron repeller grid, electron repeller grid and ion repeller grid. In this thesis, LED signal is an index of the axial loss particles.

2.6.5 Neutral particle measurement

Balmer-line emission measurement is often utilized for investigating neutral hydrogen behavior in many magnetically plasma confinement devices [30]. The principal of the Hα measurement is shown in the following chapter. Hα line emission detector consists of the Hα interference filter, a lens, an optical fiber and photomultiplier. The emission selected by the interference filter is obtained and is transferred to the photomultiplier with optical fiber. The optical signal is converted to the electronic signal in photomultiplier. High-speed camera is also used for the estimation of the neutral particles in the plasma [47-49]. High-speed camera gives us the information of the edge plasma behavior because camera can captures the 2-dimensional images which help us instantly understand the plasma behavior. This advantage is useful for control the plasma position and fluctuation, and so on. High-speed camera captures the emission with visible light range. Spectroscopic measurement can perform by using high-speed camera with interference filter.

2.7 Limiters

In the GAMMA 10 central cell, its plasma boundary is determined by using three limiters. Central limiter is located at z = +30 cm, the other (west and east limiters) are located at z = 100 cm and z = -155 cm, respectively. The central limiter is the fixed type of limiter and 400 (or 360) mm in diameters, while the another (iris limiters) are radially variable type of limiters. The diameter of the limiter can be changed within 340 mm to 400 mm.

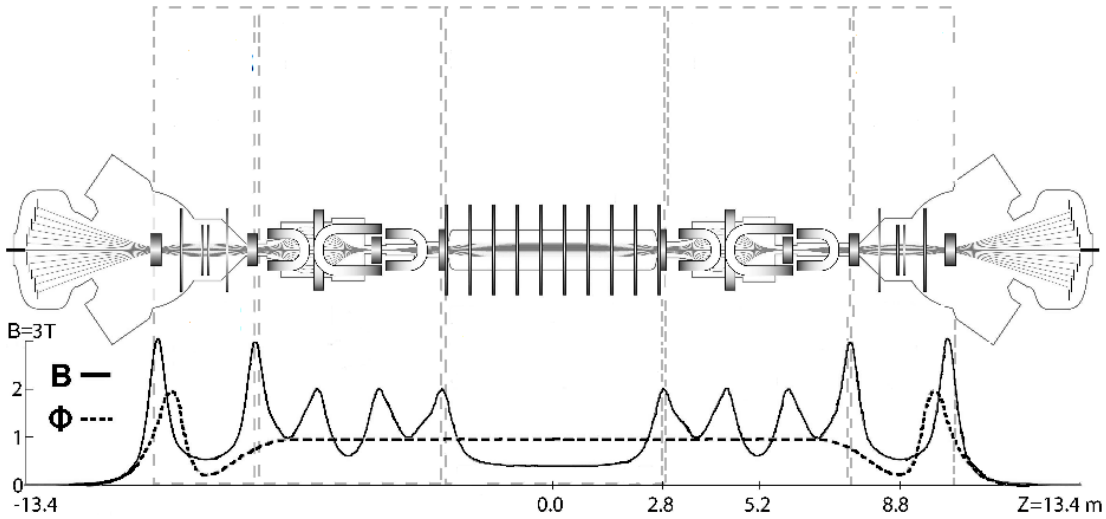

Fig. 2.1 Schematic view of the GAMMA 10 tandem mirror. It shows the vacuum vessel, coil arrangement, magnetic field profile and the potential of the plasma.

Chapter 3 Hα measurements

In this chapter, the methods of the neutral transport analysis are explained in detail. Analysis method is to couple the measured Balmer-line intensity with the simulation result by the Monte-Carlo method in this study. In consideration of the plasma parameter of the GAMMA 10 plasma, Collisional-Radiative (CR) model is employed in order to carry out this analysis. Information of spatial profile of emissivity is determined by using a Monte-Carlo simulation.

3.1 Hα measurement

In order to study behavior of neutral particles in plasma confinement devices, the diagnostics of Balmer-line emission is a useful method [30]. We employed Hα line emission whose quantum number is n=3-2, and wavelength is 656.3 nm, because this line is in visible light, easy to measure and the model for the plasma spectroscopy has been developed for estimating the neutral hydrogen density. Balmer-line is visible light, which enable us to easily measure the emission. The plasma is assumed to be optically thin enough. In consideration of the plasma parameter region of the GAMMA 10 plasma, this assumption is appropriate. The Hα emission $E\,(r)$ can be written by the next relation with the number density of level 3, $n_3(r)$ and transition probability A_{32}.

$$E\,(r) = \frac{hc}{\lambda_{H_\alpha}}\, n_3(r) A_{32} \tag{3.1}$$

where the h, c and $l_{Hα}$ are the Planck's constant, the speed of light and the wavelength of the Hα line, respectively. If $E\,(r)$ is measured, $n_3(r)$ can be obtained. Finally, the neutral density which is the number density of the ground state can be estimated by using the CR model [50-52].

3.1.1 Axial distribution of neutral particle

In order to measure the axial distribution of the neutral particles, five Hα detectors are installed at z =+100 cm, -1 cm, -71 cm, -141 cm -240 cm, and -305 cm. The axial distribution of Hα is affected by the interior components. Therefore the detector at z = +100 cm monitors the Hα emission near the west iris limiter, the detectors at z = -1 cm and -71 cm monitor that near the midplane in the central cell, the detector at z = -141 cm monitors that near the east iris limiter, the detector at z = -305 cm monitors that near the gas puffer which is mainly used for particle supply.

3.2 Collisional-Radiative (CR) model

In this model, the number density of level p is determined from the electron temperature, density and number density of the ground state. The processes of radiative-transition, recombination, electron impact excitation, ionization and three-body collisional recombination are considered as atomic processes. The schematic drawing of the atomic processes used in the CR model is shown in Fig. 3.2. The number density of level p of the atomic hydrogen n_p is represented by the following rate equation.

$$\begin{aligned}\frac{d}{dt}n_p = & -n_p n_e S(T_e,p) - n_p n_e \sum_{p\neq q} X(T_e,p,q) \\ & - n_p \sum_{q<p} A_{pq} + n_e \sum_{p\neq q} n_q X(T_e,p,q) \\ & + \mathrm{n_i} n_e \alpha(T_e,p) + n_e \sum_{q>p} n_q A_{pq} + n_i n_e \beta(T_e,p)\end{aligned} \tag{3.2}$$

where *ni*, *ne* and *Te* are the hydrogen ion density, electron density and electron temperature, respectively. $S(T_e,p)$, $X(T_e,p,q)$, $\alpha(T_e,p)$ and $\beta(T_e,p)$ are the rate coefficients for the ionization, collisional excitation, three-body recombination and radiative-recombination, respectively. In a level of $p \gg 1$, where a local thermal equilibrium can be assumed, the relationship among n_i, n_e and n_p can be rewritten by Saha's ionization equation.

$$n_p = n_p^E \tag{3.3}$$

$$\frac{n_i n_e}{n_p^E} = \frac{2g_+}{g_p}\frac{(2\pi m_e \kappa T_e)^{3/2}}{h^8} exp\,(\frac{E_p}{\kappa T_e}) \tag{3.4}$$

where g_+, g_p, κ and m_e, are the multiplicity of ion and level p, Boltzmann constant and mass of electron, respectively. Moreover, by solving the simultaneous equations of $p-1$ unknowns, n_p can be rewritten as follows,

$$n_p = R_0(p) n_i n_e + R_1(p) n_H n_e \tag{3.5}$$

The first and the second terms of the right hand side of the above equation are the recombination process between ion and electron with rate coefficient $R_0(p)$ and excitation of hydrogen atom with $R_1(p)$, respectively. n_H is the hydrogen atom density. Since the electron temperature in GAMMA

10 is obtained to be higher than 10 eV, the recombination term in Eq. 3.5 can be neglected. Moreover, the effect of the direct dissociative excitation reaction of hydrogen molecule is not negligible when the density of hydrogen atoms in excited levels is estimated, since the electron density in GAMMA 10 is lower than $10^{19}\mathrm{m}^{-3}$ [30]. Eq. 3.5 is, then, rewritten by using a rate coefficient for the dissociative excitation of hydrogen molecule $R_2(p)$ and its density n_{H_2}

$$n_p = R_1(p) n_H n_e + R_2(p) n_{H_2} n_e \tag{3.6}$$

If the plasma density and the electron temperature are obtained, R_1 and R_2 are derived from this equation. In order to determine the neutral hydrogen density, Monte-Carlo simulation is carried out.

3.3 Coupling with Monte-Carlo simulation

Monte-Carlo method is often used for determining the neutral density in plasma confinement devices. The intensity of Balmer-line emission is determined with use of the calculated neutral density and CR-model, and then is normalized with the experimental results obtained by the Hα detector. If Balmer-line emission is absolutely calibrated the absolute value of the neutral density is also obtained from this method. In the measurement of the detector, only the information of the Hα emission near the sight line of the detector is obtained. By the combination of Hα emission measurement and Mote-Carlo simulation, the ionization rate of the neutral particles and the hydrogen recycling is determined in the whole area of central cell. From the analysis, the radial and axial profile of the neutral density is estimated.

It is noted that such analysis method become a more useful method according to the recent development of computer performance. In the Monte-Carlo technique, the Boltzmann equation describing the neutral particle distribution is time-independently solved. This indicates that the static-condition is assumed for the Monte-Carlo calculation. In GAMMA 10, the Monte-Carlo simulation code (DEGAS) has been applied. The physical process and the computational technique on DEGAS are shown in Appendix A. The DEGAS application to GAMMA 10 and recent progress about the simulation technique is precisely explained in the next section.

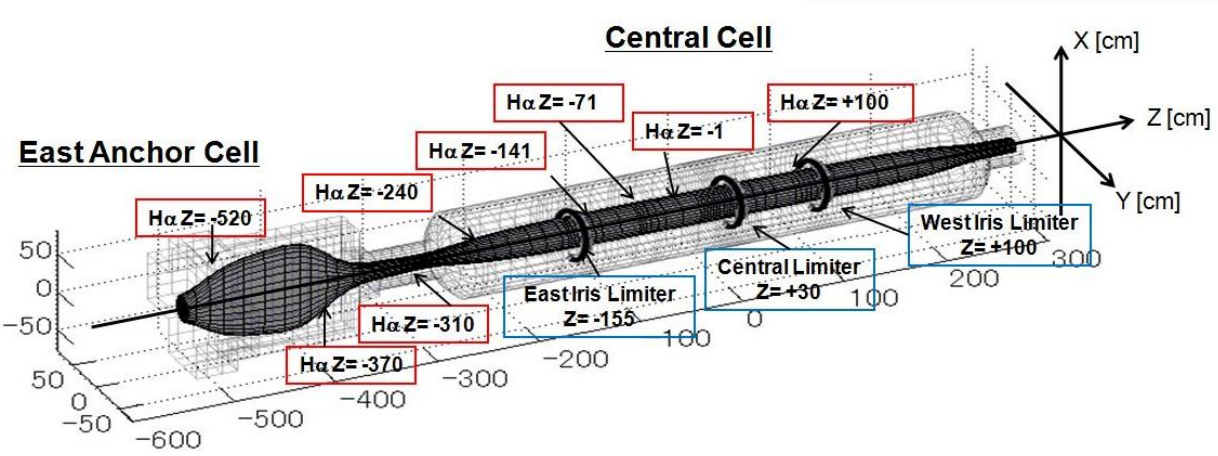

Fig. 3.1 Location of the Hα line emission detector

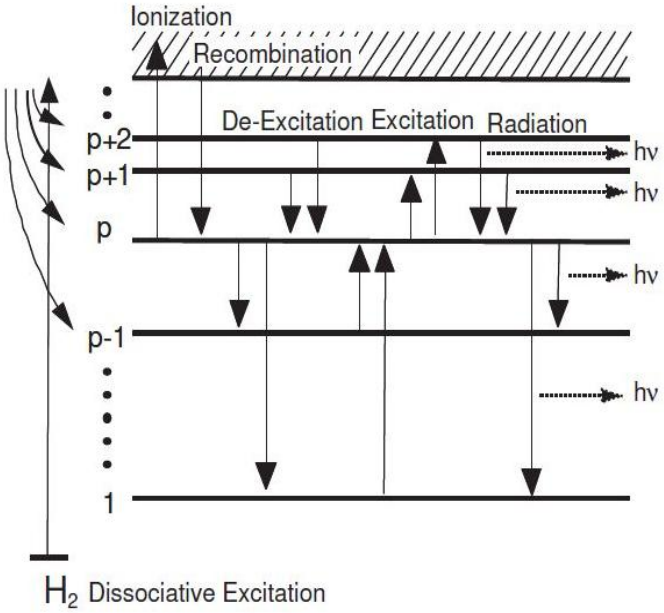

Fig. 3.2 Schematic view of CR-model process.

3.4 Monte-Carlo simulation code (DEGAS)

The DEGAS code is a numerical calculation code that simulates the transport of multiple species neutral particles in three-dimensional plasma by using a Monte-Carlo technique. The numerical process follows on Boltzmann equation. This code was originally developed at the Princeton Plasma Physics Laboratory (PPPL) and has widely used for the estimation of the profiles of the density and temperature of the neutral particles in many magnetic confinement devices.

It has been reported that the density profile of neutral hydrogen atoms calculated by the DEGAS code was significantly different from the experimental results in the case that the plasma density was less than $10^{19}\mathrm{m}^{-3}$ [30], since this code was developed for the simulation of the high plasma density region such as divertor. This discrepancy was attributable to the production of hydrogen atoms at excited levels by the direct-dissociation of hydrogen molecules upon electron impact. The dissociative-excitation reactions of neutral hydrogen molecules are additionally included so as to calculate low density plasma in the plasma edge region for applying the DEGAS code to the GAMMA 10 plasma. This modification is explained in appendix A.

The version 35 of DEGAS code (DEGAS35) was firstly installed for the simulation of the central cell. The meshes for this code are constructed as a 2-dimensional axis. Mesh configurations and plasma parameters in the cell of simulation space are assumed to be symmetry axis. The schematic image of mesh for DEGAS35 is shown in Fig. 3.3.

The version 63 of DEGAS code (DEGAS63) has been applied for investigation of the neutral transport due to the non-axisymmetric structure of the wall geometry and plasma parameter, and the non-uniform distribution of the neutral sources. In the DEGAS63 code, the mesh is completely formed as 3-dimensional configuration in the schematic view shown in Fig. 3.4.

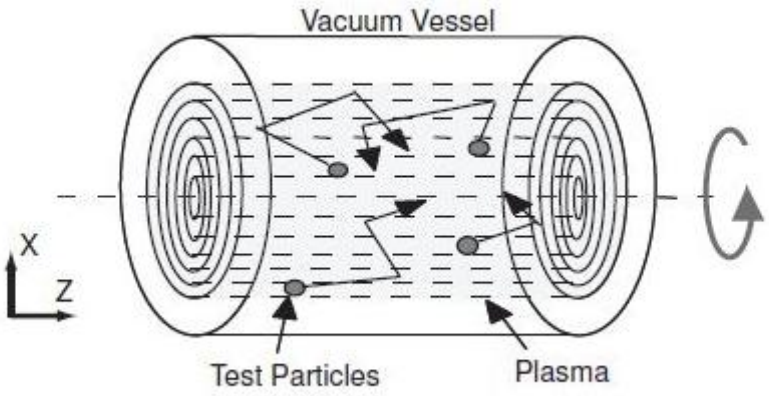

Fig.3.3 Schematic view of the plasma mesh model used in DEGAS 35 simulation.

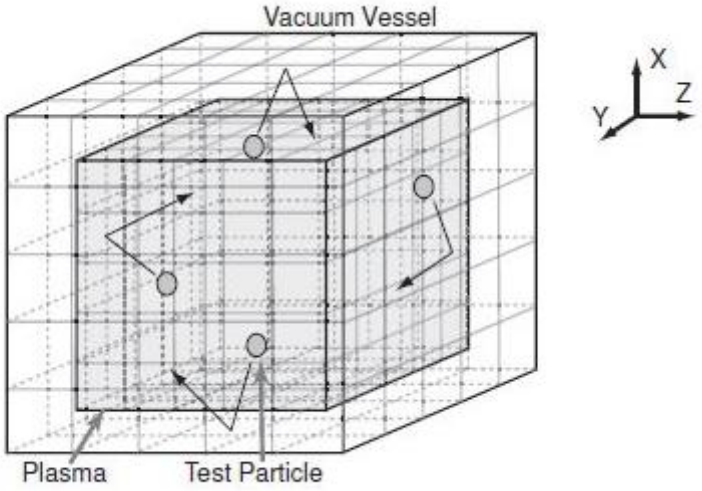

Fig.3.4 Schematic view of the plasma mesh model used in DEGAS 63 simulation.

Chapter 4 Particle Control Based on Particle Balance in the C-ECRH Experiments

In this chapter, the cause which often degrades the plasma parameters during the ECRH injection for additional heating is investigated from a viewpoint of particle balance. The purpose of this study is to clarify the mechanism of the degradation of the plasma parameters during the ECRH injection. Optimization of the ECRH experimental condition was also investigated based on the particle balance.

4.1 Typical experimental results during ECRH injection

In the standard sequence of the GAMMA 10 plasma production, initial plasma is produced by the magneto-plasma-dynamic (MPD) guns installed on both end of GAMMA 10. The fuel particles are supplied by the gas puffer. The main plasma is build up and sustained by ICRF heating. Therefore a significant difference occurs between the ion temperature and the electron temperature in the plasma. ECRH is injected in the central cell in order to prevent the electron drag caused by this temperature difference. However the degradation of the plasma performance is occasionally observed in the ECRH period. Not only the diamagnetism but also electron line density was decreased in that period. It is speculated that the degradation of the plasma performance is caused by the plasma particles loss which is enhanced by ECRH injection [7].

The typical experimental results such as diamagnetism, electron line density, intensity of the soft X-ray, signal of end loss electron, radial ion flux, in the C-ECRH injection period are shown in Fig. 4.1. The timing of blue area is the C-ECRH injection period. In figure 4.1, in the case (a) that the diamagnetism increased, the electron line density did not decrease, and the signal of ISP and LED. On the other hand, in the case (b) that the diamagnetism decreased, the electron line density decreased, and the both signals of ISP and LED increased. These above results indicated that the degradation of the plasma parameters have a correlate with the loss particles. The proper control of particle balance is an important key for the achievement of high performance plasma.

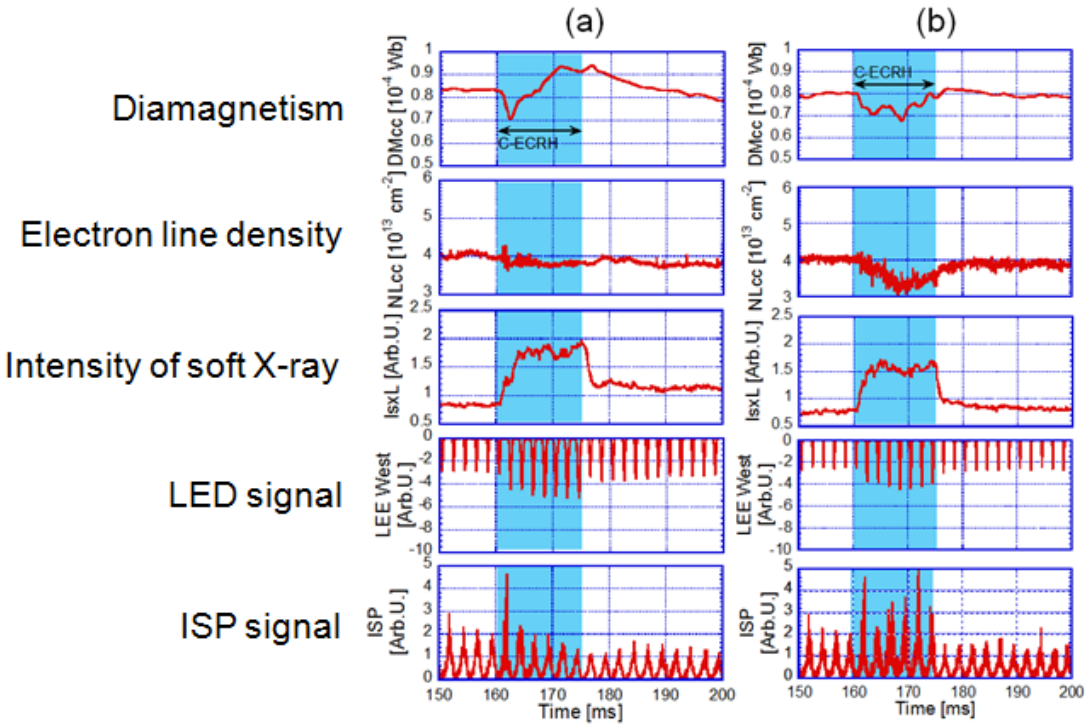

Fig. 4.1　Typical experimental results during C-ECRH
(a) diamagnetism increasing　(b) diamagnetism decreasing

4.2 The assumed mechanism of enhancing the loss particles

We considered how the electron was expelled during the C-ECRH injection. When the ECRH is injected to the region with the magnetic gradient, the electron is expelled in weak direction of the magnetic field. This is a mechanism into which the electron is expelled. Schematic view of this mechanism is shown in Fig. 4.2. The axial-confining potential improved the plasma performance because the axial escaping electron was plugged by the axial-confining potential.

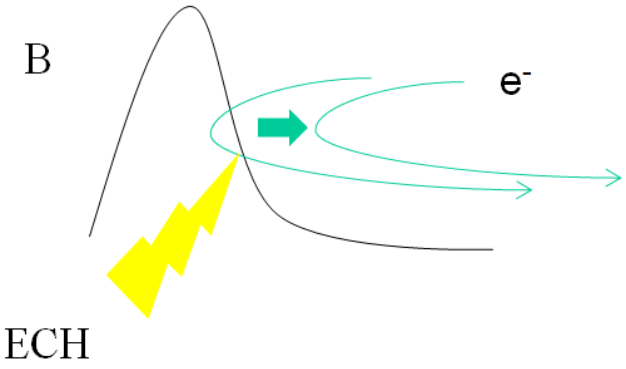

Fig. 4.2 schematic view of the mechanism of expelling the electron

4.3 Particle balance

In order to discuss the particle confinement in mirror device, different from the torus devices, not only the radial particle transport but also the axial transport along the magnetic field line should be considered. The particle balance equation under mirror configuration can be represented as follow,

$$\frac{\partial n}{\partial t} = -\nabla \Gamma_{\perp} - \nabla \Gamma_{\parallel} + s \tag{4.1}$$

In this equation, the rate of change of the density (n) equals the sum of the particle source (s) and the negative of the divergence of the radial and axial particle flux ($\Gamma_{\perp}$and $\Gamma_{\parallel}$). The radial and axial particle flux can be expressed by integrating that particle balance equation with a plasma volume.

$$\frac{\partial N}{\partial t} = -\Gamma_{\perp} - \Gamma_{\parallel} + S \ , \tag{4.2}$$

where N and S are the total particle number and the total particle source, respectively. In consideration of this equation, as long as increasing of the loss term $(\Gamma_{\perp} + \Gamma_{\parallel})$ causes the

degradation of the plasma parameters, it is necessary to increase the particle source (S), or to decrease the loss term in order to prevent the degradation of the plasma performance.

4.4 Suppression of the loss particle by using axial-confining potential

In order to understand the physical mechanism of the degradation of the plasma during the C-ECRH, the experiment of the C-ECRH injection without the confining potential was performed in order to verify the effect of the C-ECRH. The two types of time behavior of the plasma parameters are compared in Fig. 4.3. One is “only C-ECRH” that the experiment is performed without the confining potential. The other is “with all ECRHs” that the experiment is performed with the confining potential. In this experiment, the signal of LED and ISP increases at the same time. These results mean that the particle loss causes the degradation of the stored energy. Therefore, it is considered that the degradation of the plasma is induced by the enhancement of the particle loss with C-ECRH.

On the basis of these results, the optimized condition of the experiment was investigated. As a result, the Diamagnetism measured in the central cell (DMcc) was increased during the C-ECRH injection with P/B-ECRH even though the electron line density measured in the central cell (NLcc) was slightly decreased. Furthermore the signal of ISP and ESPs was decreased at the same time. This means that the bad influence induced by the C-ECRH is significantly suppressed by the axial-confining potential. From the experimental results, the degradation of the plasma performance was thought to be induced by the plasma particles loss. In the case that the axial-confining potential plugged the axial escaping particle, the plasma performance was improved.

Figure 4.4 shows the difference of loss particle between before and after C-ECRH injection. In this figure, the horizontal axis indicates the ratio of the average of ISP signal during C-ECRH injection to the average of ISP signal before C-ECRH injection. In the case that the value of the ratio on the horizontal axis is more than unity, the radial loss is determined to be increasing. The right side of vertical axis indicates the ratio of the average of LED signal during C-ECRH injection to the average of LED signal before C-ECRH injection under the condition of without the axial-confining potential (◆). In the case that the value of the ratio on the vertical axis is more than unity, the radial axial loss is determined to be increasing in the same way. With axial-confining potential (●), the LED signal was increased by the expelled electron during P-ECRH injection. The discrepancy of the LED signal between before and during C-ECRH injection could not be compared because the expelled electron induced by P-ECRH is dominant. Therefore, with confining potential, the ratio of the average of LED signal during C-ECRH injection to the average of LED signal without C-ECRH was plotted. In this case, the value of the ratio on the vertical axis was nearly equal unity. This result means that C-ECRH injection did not cause the increasing the axial loss. Without axial-confining potential (◆), the ratio of the average of two ISP signals was plotted in more than unity on vertical and horizontal axis. This result indicated that axial and radial loss flux

increased during C-ECRH injection. On the other hand, with axial-confining potential (●), the ratio of two ISP signals on the horizontal axis was plotted in less than unity. This meant that the radial loss ion flux decreased during the C-ECRH injection.

Furthermore the value of the ratio on the vertical axis was nearly equal unity. From above results, not only axial loss but also radial loss was suppressed by using the axial-confining potential. The mechanism of the radial ion loss caused by axial electron loss was supported by these results.

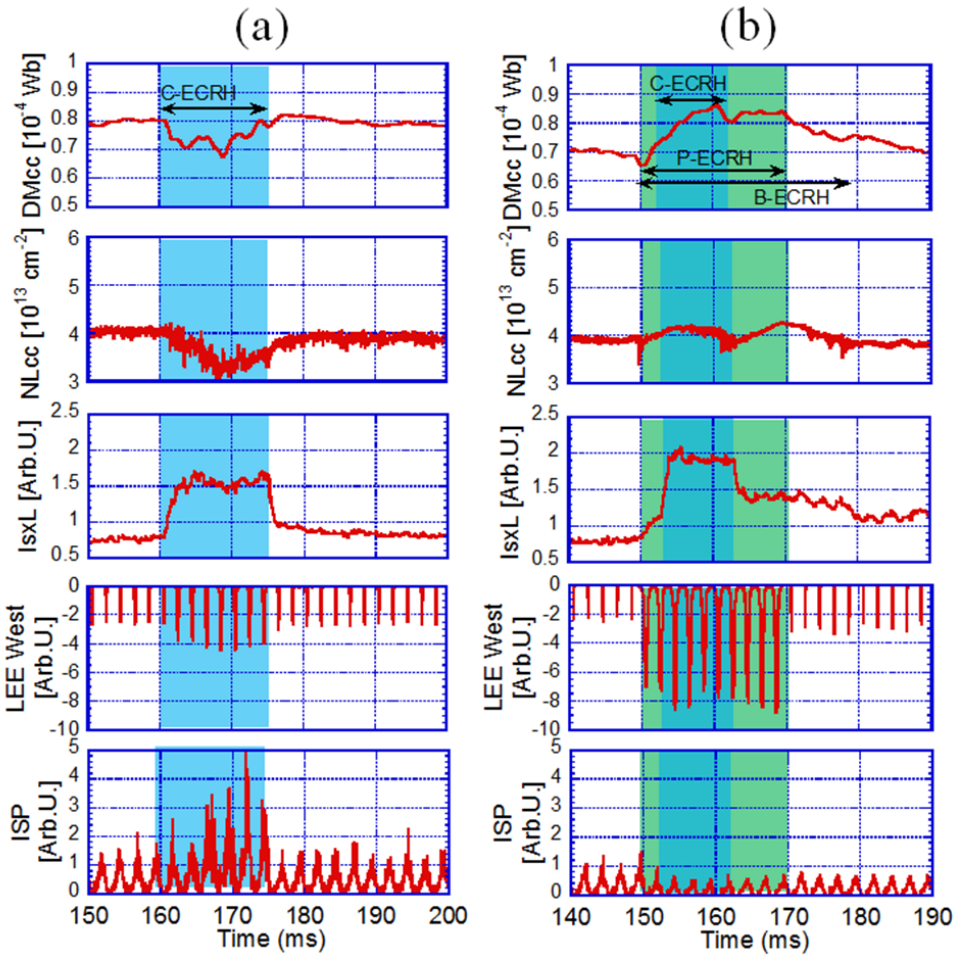

Fig. 4.3　Time behavior of the plasma parameter during C-ECRH injection.
(a)without confining potential　(b)with confining potential

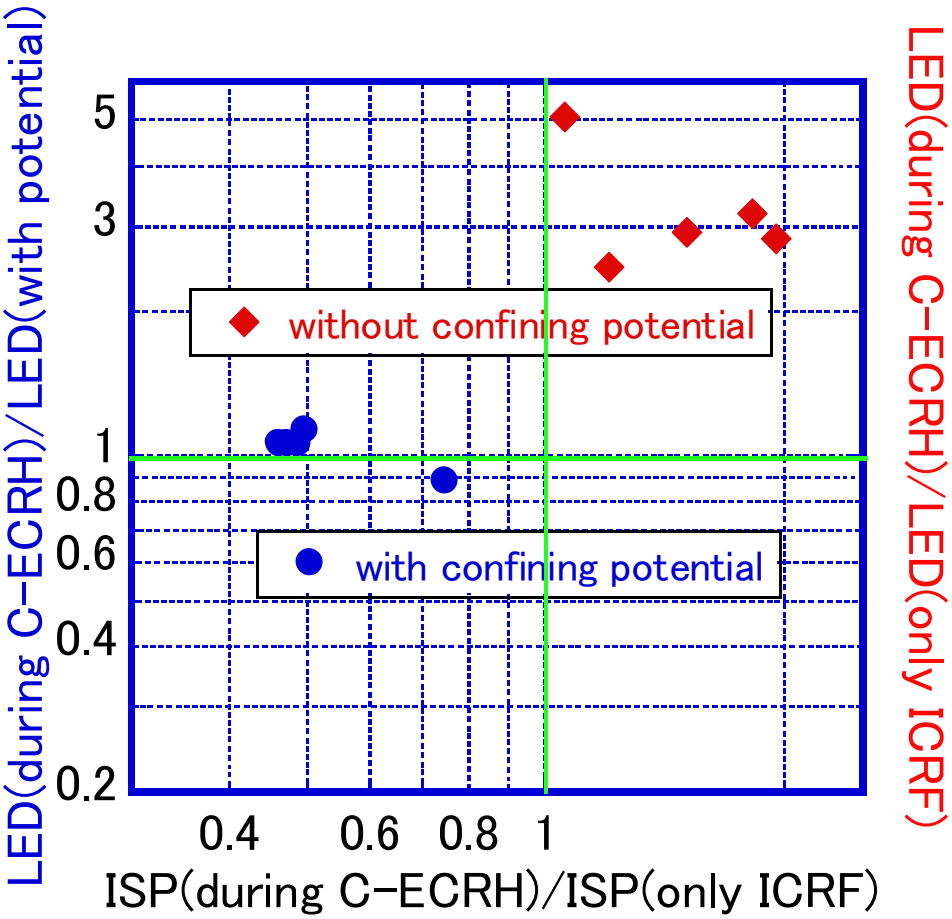

Fig. 4. 4　Comparison loss particles between before and during C-ECRH injection.

4.5 Control of the amount of the limiter recycling source

In the C-ECRH experiments, it has been reported that the plasma performance has a dependence on the diameter of the iris limiters [53, 7].

In the case with ϕ = 350 mm, as shown in Fig. 4.5(a), the diamagnetic signal (DMcc) is degraded during C-ECRH injection. The electron line integrated density (NLcc) measured at the central-cell decreases just after the start of the ECH pulse. However the plasma collapse was prevented. On the other hand, in the case with ϕ = 380 mm, as shown in Fig. 4.5(b), the plasma collapses when the C-ECRH injected. This result indicates that particle source from limiter recycling decreased in the case that iris limiter diameter is large and the proper particle balance could not be sustained. Therefore the plasma collapse was caused by decreasing the particle source. On the other hand, particle source from limiter recycling was increased in the case that iris limiter diameter was small. The increasing of the particle source prevented the collapse caused by the increasing of the particle loss during the C-ECRH injection. How plasma parameters depend on the limiter diameter is investigated. In Fig. 4.6(a), NLcc and DMcc are plotted as a function of the diameter of the iris limiters. In this case, the diameters of both iris limiters are kept at the same diameter. It is confirmed that NLcc tends to increase according to the reduction of the diameter of the iris limiters. On the contrary, DMcc tends to decrease according to the reduction of the diameter of the iris limiters. In Fig. 4.5 (b), Hα intensity decreases with the limiter diameter, which indicates that the hydrogen recycling is enhanced due to the reduction of the limiter diameter. The dependence of Hα intensity in the west iris limiter is stronger than that in the east, since the position of the Hα emission detector is much closer to the west iris limiter.

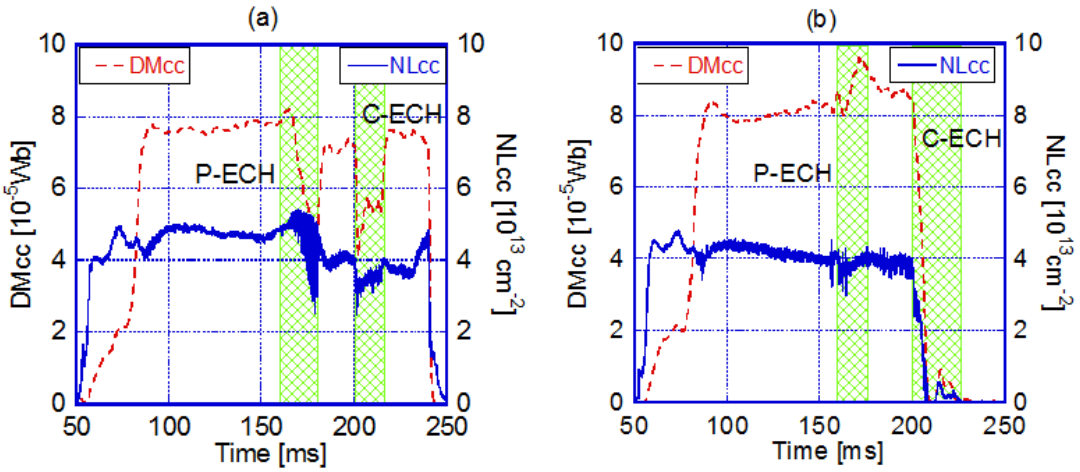

Fig. 4.5　Changing the iris limiter diameter experiments.
Iris limiter diameter：(a) ϕ 350mm (b) ϕ 380mm

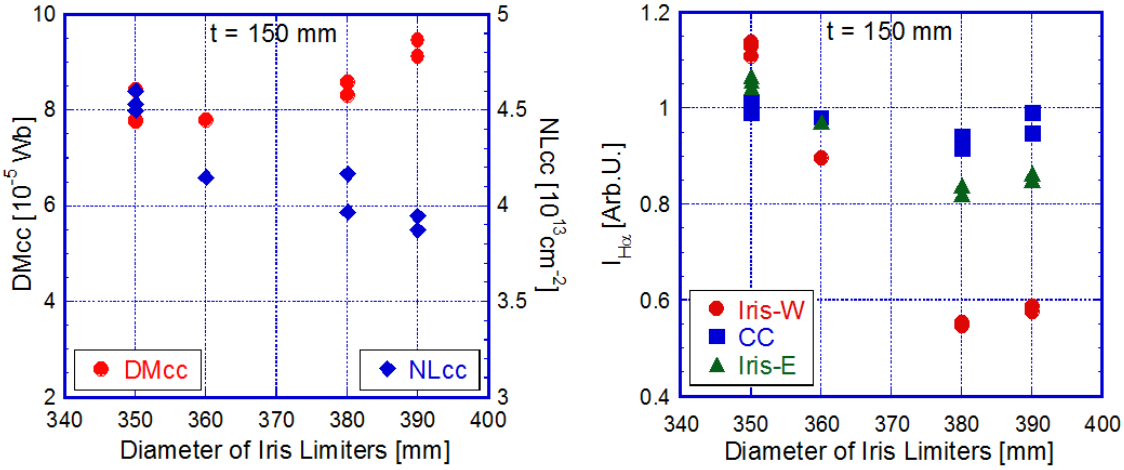

Fig 4.6　Dependence of limiter diameter.
(a) Diamagnetism and electron line density (b) Hα line emission intensity

4.6 Dependence on the through put of the gas puff

In this section, the dependence of the plasma parameter on amount of particle from gas puffer was investigated in the C-ECRH experiments. The time behavior of the plasma parameters for the dependence of the amount of gas puff was shown in Fig. 4.7.

Figure 4.7 shows that the value of reduced is increasing with decreasing the plenum pressure (P_{plenum}) of the gas puffer. If the reproducibility on the discharge is assumed, the amount of the loss particle induced by C-ECRH injection is same amount on each discharge. Furthermore the plasma parameters depend on the plenum pressure. These results indicate that the degradation of plasma parameters was caused by the increasing the loss particles. Note that these results were observed in almost continuous discharges. Therefore uncertainly of the neutral particle behavior, such as wall condition, can be ignored.

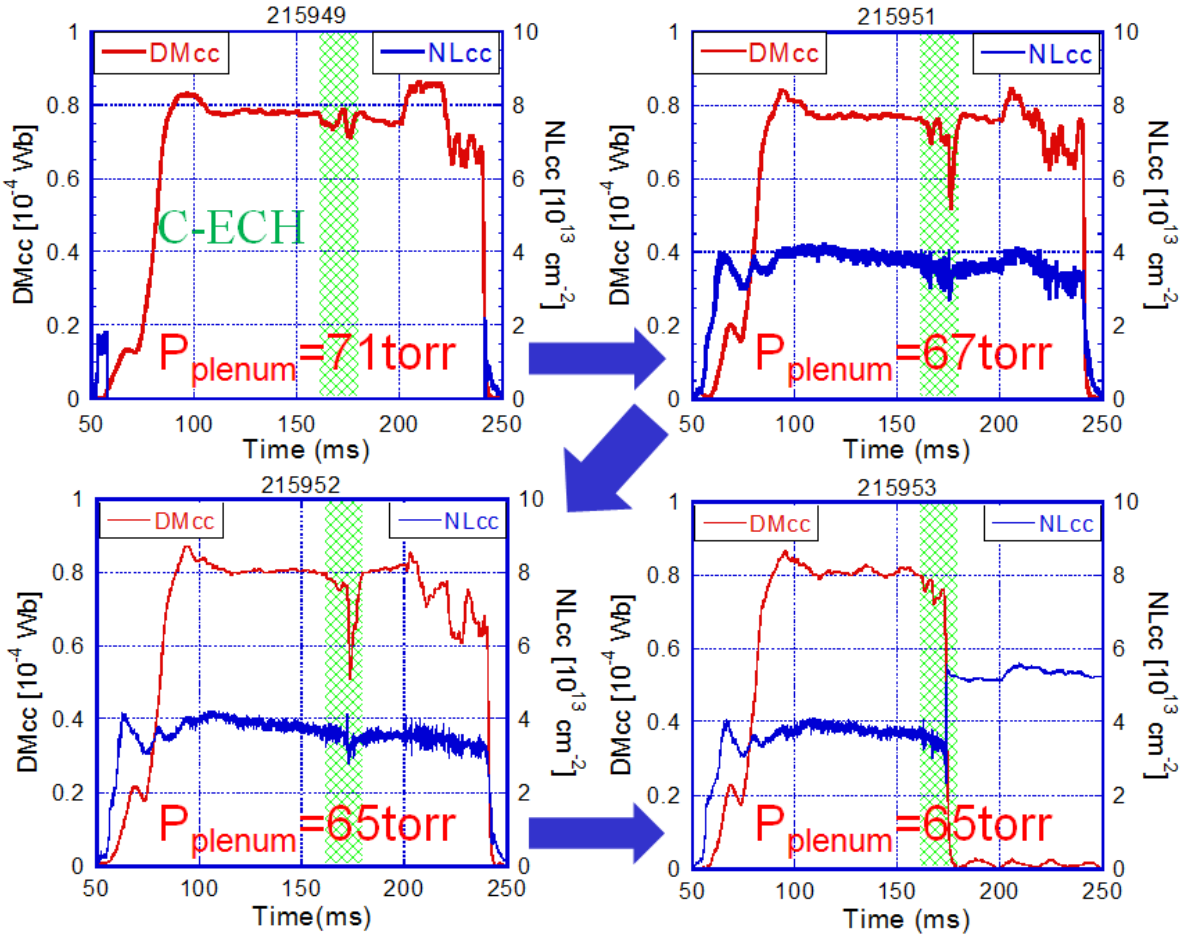

Fig. 4.7　Dependence of the plasma performance on the plenum pressure.

＊Electron line density at left upper graph is could not measured correctly

4.7 Dependence of ICRF power

In this section, the dependence of the plasma parameter on the power of ICRF was investigated in the C-ECRH experiments. Figure 4.8 shows the time behavior of the plasma parameter in the C-ECRH experiments for investigating the dependence of the ICRF power (P_{ICRF}). In the case that plasma was sustained during the C-ECRH injection (#215932, #215935), NLcc was significantly decreased at the same time. These results also indicate that the degradation of plasma parameter was caused by the increasing the loss particles, and that the sustainment of the plasma depends on the intensity of ICRF power. In the case that the ion temperature heated by ICRF is not enough, the recycling coefficient was small. Decreasing the recycling coefficient indicate the decreasing the neutral particle source due to recycling. From above results, the plasma collapsed during the C-ECRH injection in the case that the intensity of ICRF power is low. In the next section, the correlation between the recycling coefficient and ion temperature is explained in detail.

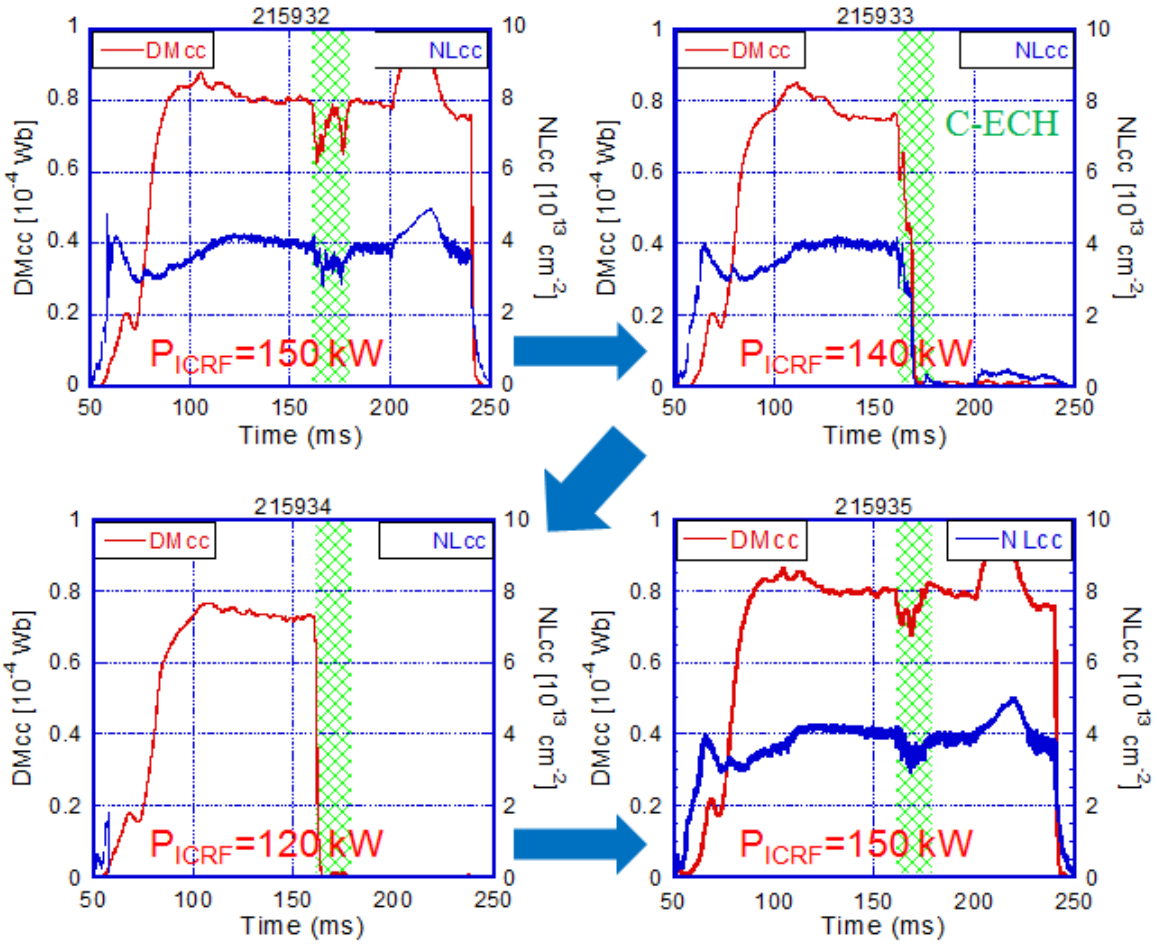

Fig. 4.8 Dependence of the plasma performance on ICRF power.

＊Electron line density at left bottom graph is could not measured correctly

4.8 Correlation between the recycling coefficient and ion temperature

Hydrogen atom escaping from the plasma through the charge exchange process hits the vacuum vessel wall. Then impinging atom reflects on the wall or desorbs the particle absorbed on the wall. The reflection coefficient of charge exchange neutral particle reflection on the wall depends on the energy of the incident particle. The dependence of the reflection coefficient on the incident particle energy has been reported by W. Eckstein and H. Verbeek [54]. Figure 4.9 shows the reflection coefficient R_N on the incident particle energy of the hydrogen beam in the case that the target material is iron. On the basis of this results, by using the equation as follows, the dependence of the reflection coefficient on the ion temperature are shown in Fig. 4.9 in the case that isotropic plasma in the 3-dimensional is assumed.

$$\langle R_N \rangle = \frac{\int R_N(E) f_i(E, T_i) dE}{\int f_i(E, T_i) dE}, \tag{4.3}$$

where $f_i(E, T_i)$ is ion distribution function. In the case that the ion temperature is 0.6, 1 keV, $\langle R_N \rangle$ is 0.34, 0.29, respectively. Hydrogen recycling has been evaluated by numerical simulation based on the pressure balance equation in GAMMA 10 [10]. The hydrogen analysis has been investigated by the gas dynamic pressure analysis. Based on this analysis, the recycling coefficient can be determined as follows,

$$\begin{aligned} \gamma &= \frac{reflected\ atoms + desorbed\ molecules\ \times 2}{energetic\ incident\ atoms} \\ &= R_N + R_D \end{aligned} \tag{4.4}$$

where R_D are desorption coefficients. We referred to the W. Eckstein and H. Verbeek model for the reflection coefficient [54]. Figure 4.10 shows the dependence of the recycling coefficient on the average ion temperature. It has been observed that the recycling coefficient was more than unity in the ion temperature range of the standard operation of the GAMMA 10 experiments. Positive correlation between the recycling coefficient and ion temperature is clarified.

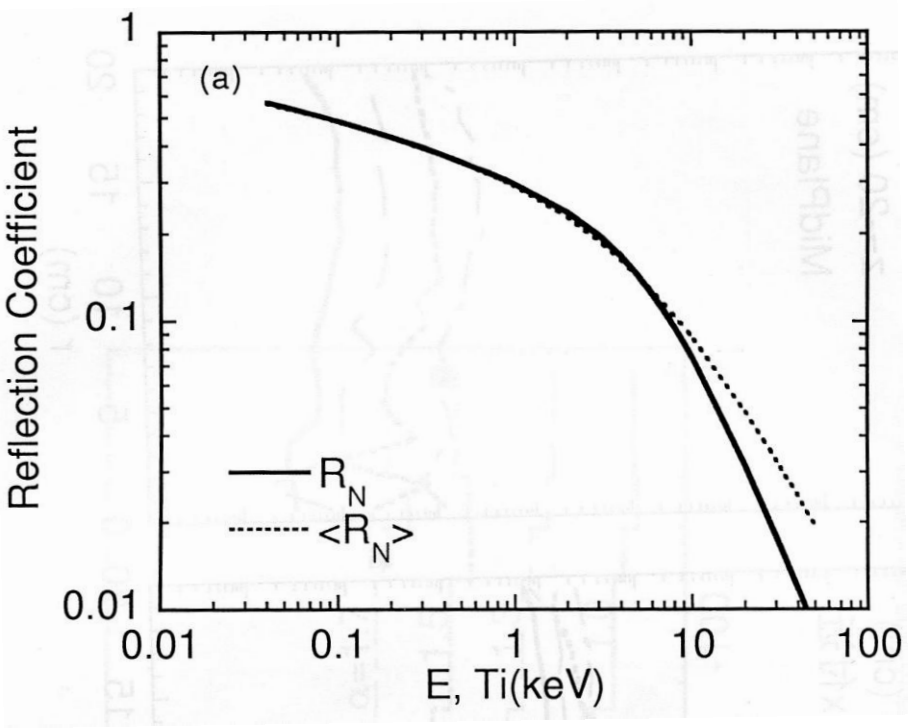

Fig. 4.9 Dependence of Reflection coefficient on the incident particle energy or the ion temperature

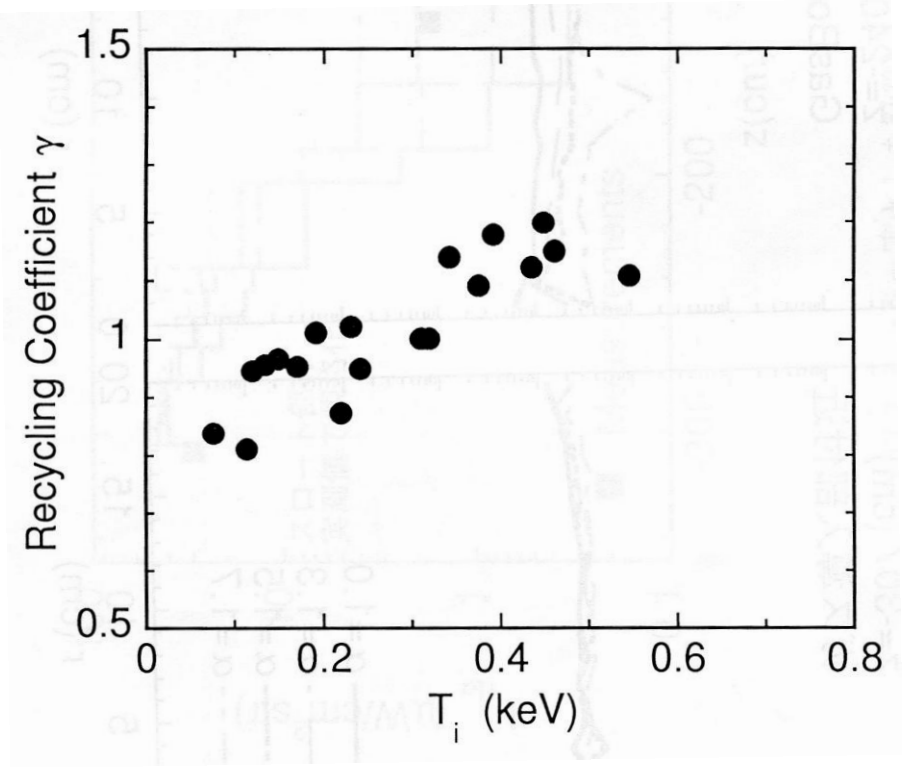

Fig. 4.10 Dependence of the reflection coefficient on the ion temperature

4.9 Evaluation of generated particles for the plenum pressure or ICRF power

The dependence of the plasma sustainment on the plenum pressure and ICRF power was evaluated as described in section 4.7. It is clarified that the recycling coefficient has a correlation on the ion temperature in section 4.8. Therefore it is speculated that the RF-induced recycling has a dependence on the intensity of ICRF power. We investigated how these conditions depend on the amount of the generated particles by using the Hα line emission intensity. Figure 4.8 shows the dependence of Hα emission intensity on the plenum pressure (a) or ICRF power (b). In this measurements, we used the Hα detectors installed at throat near the gas puffer (z = -310 cm), and installed at mid-plane in the central cell (z = -1 cm). As shown the figure 4.8, the Hα intensity depends on the plenum pressure or ICRF power in the same way. These results indicated that the particle production depends on the plenum pressure or ICRF power. From above results, the amount of the generated particles can be controlled by changing the plenum pressure or ICRF power.

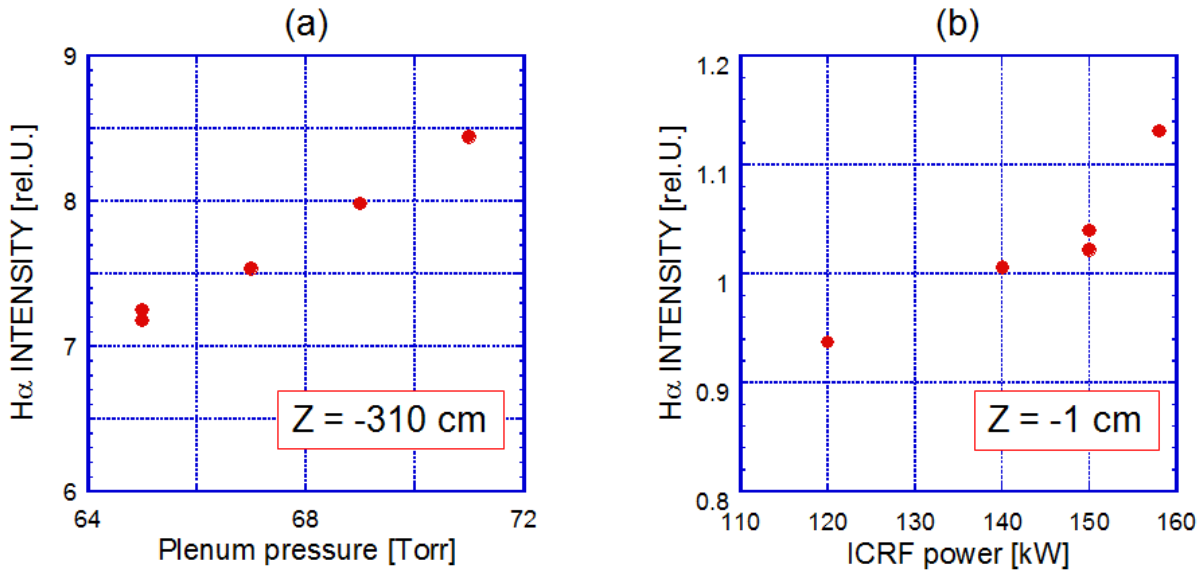

Fig. 4.8 Dependence of Hα emission intensity on the plenum pressure (a) or ICRF power (b).

4.10 The evaluation of the generated particles based on the DEGAS code

The dependence of the plasma sustainment to the diameter of iris limiters, the ICRF power, and the amount of gas puffer was discussed based on the measurement of Hα line emission detector. However the evaluation of the amount of gas in each experimental condition could be discussed only at near the Hα detector. By using neutral particle transport simulation (DEGAS), the amount of the gas was evaluated in the whole area of the central cell. In this analysis method, the particle source was given on the interior components, such as limiter. The neutral particle density profile was calculated by the DEGAS code for obtaining the Hα emission intensity on the z axis. The Hα line emission intensity calculated by the DEGAS code was compared with the Hα emission intensity obtained by the Hα detector near the particle source (z= 100, -1, -141, -305 cm). The calculation results were normalized in the axial distribution of the Hα emission intensity obtained by experimental results. The simulation in this study was carried out in the case that the particle source was given each limiter, GP#3. The amount of the generated particle from the recycling on the limiter and/or gas puffer was evaluated.

The mesh model reproducing the whole area of the central cell was necessary in order to discuss the generated particles in the central cell. The mesh model was improved for this study. Fully 3-dimentional mesh model used in this study is shown in Fig. 4.9. Plasma configuration is also shown in Fig. 4.10. It has been reported that the configuration of the anchor cell affected the neutral particle behavior in the central cell. Not only the central cell but also the anchor cell is necessary for evaluation of the generated particles in the central cell.

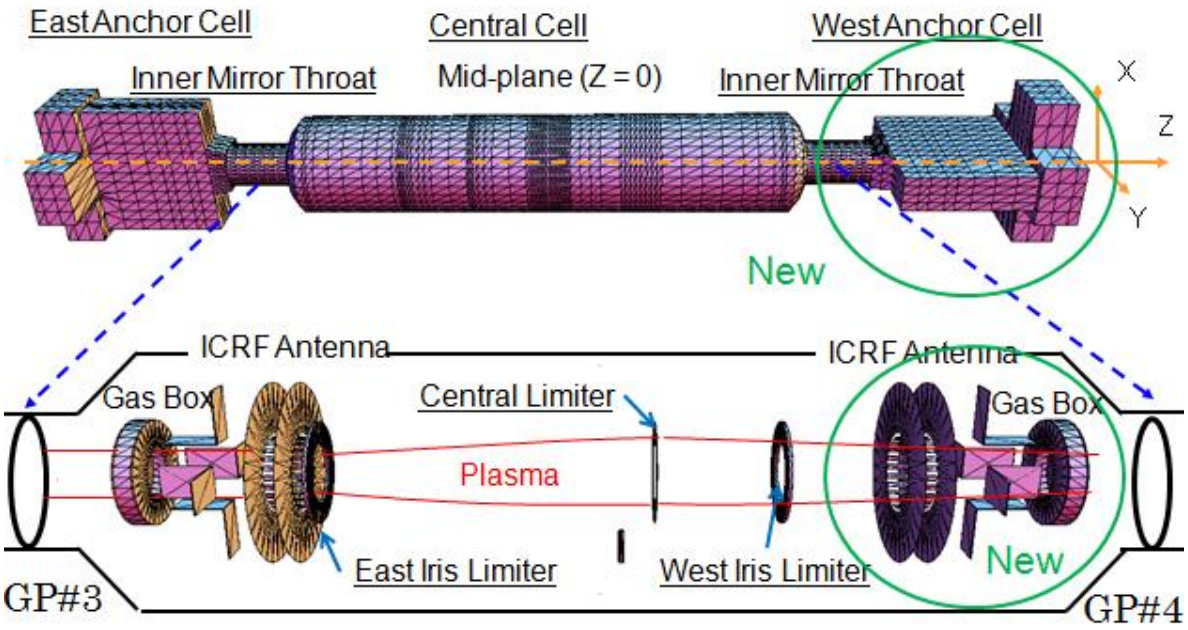

Fig. 4.9 Central cell and anchor cell integrated mesh model.

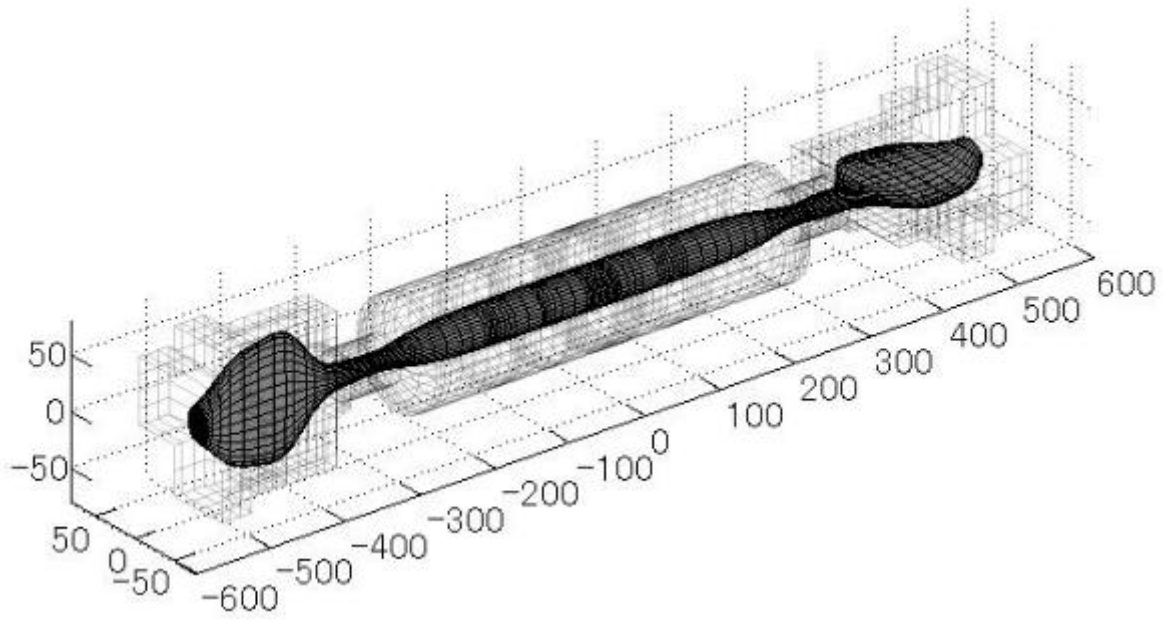

Fig. 4.10 Plasma configuration.

4.10.1 The generated particles from limiter recycling

The particle source was given on the each limiter (cc-limiter, east and west iris limiter). The limiter position was shown as green hatched area at 100 cm, 30 cm, and -155 cm in Fig. 4.11. The amount of the generated particles was compared between the condition that limiter diameter is larger and the condition that limiter diameter is small. The amount of generated particle was evaluated for the dependence on the plasma sustainment based on the Hα line emission intensity in the two cases that the iris limiter diameter is ϕ=340 mm (a) and ϕ=400 mm (b). In the case of (a), the plasma was sustained. In the case of (b), the plasma was collapse. Figure 4.11 shows the distribution of the generated particles on the z axis in each case of the limiter diameter. The simulation results indicate that the amount of the generated particles in the case of ϕ=340 was about 1.3 times larger than that in the case of ϕ=380.

4.10.2 Dependence on the ICRF power

The particle source was also given on the each limiter (cc-limiter, east and west iris limiter) in this subsection. The limiter position was shown as green hatched area at 100 cm, 30 cm, and -155 cm in Fig. 4.12. The amount of the generated particles was compared between the conditions that ICRF power is high (a) and low (b). In the case of (a), the plasma was sustained. In the case of (b), the plasma was collapse. In the simulation results, the amount of the generated particles in the case of 150 kW was about 1.22 times bigger than that in the case of 120 kW. The axial distribution of the generated particles in this simulation is shown in Fig. 4.12.

4.10.3 Dependence on the plenum pressure of the gas puffer

In order to evaluate the generated particles against the plenum pressure of gas puffer, the neutral particle was given on the GP#3, axial distribution of the generated particle was calculated in the case of the high plenum pressure (a) and low plenum pressure (b). The amount of the generated particles in the case of 71 Torr was about 1.22 times bigger than that in the case of 65 Torr. The axial distribution of the generated particles in this simulation is shown in Fig. 4.13.

4.11 The effect of the generated particle on the plasma sustainment

From the evaluation in the previous chapter, the DEGAS code enables us to evaluate the generated particles under the various experimental conditions in fully 3-D simulation. Furthermore the generated particles can be controlled by the changing the diameter of the iris limiter, ICRF power and the plenum pressure of the gas puffer. In addition, it seems that the around ten percent of the increasing the generated particle is effective to prevent the plasma collapse. The same results were given from the different particle source such as limiter recycling or gas puffer. We can give a quantitative evaluation for the particle supply. These results indicated that the DEGAS code can be a valuable tool for optimization of the experimental condition under the various particle sources. From above results, we can contribute to the study of controlling the neutral particles for the complicated devices such as helical type devices, or tokamak device as represented by ITER.

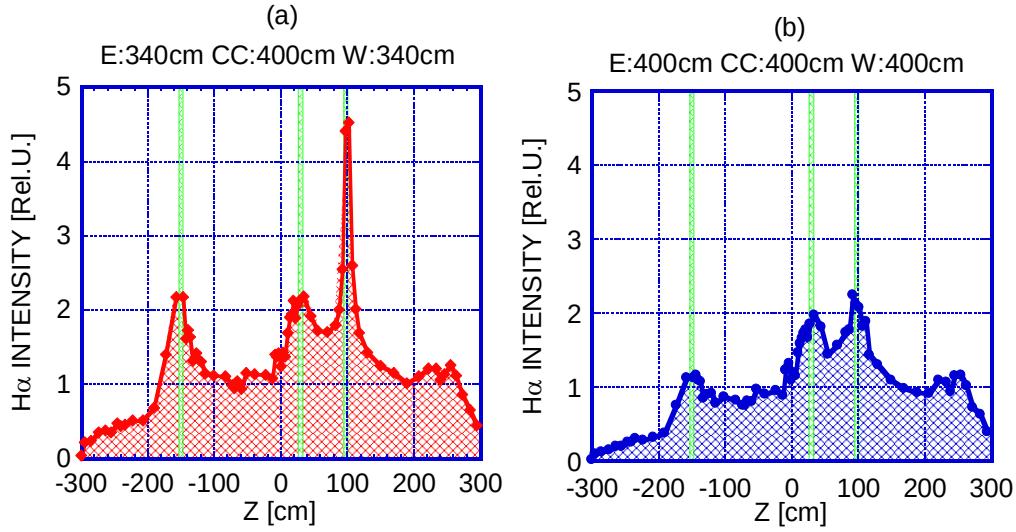

Fig. 4.11　z axis distribution of generated particle on the limiter diameter.
Limiter diameter　: (a) 340 mm　(b) 400mm

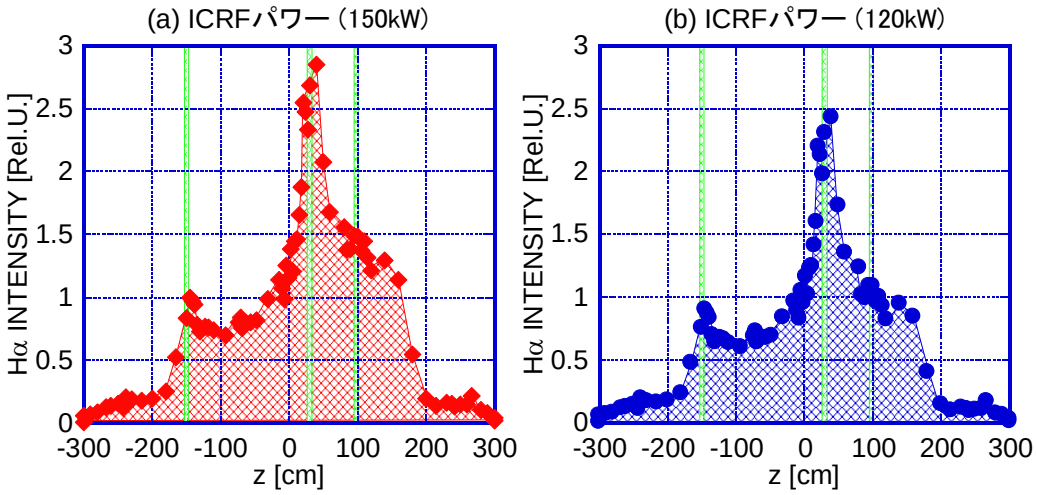

Fig. 4.12　z axis distribution of generated particle on the ICRF power.

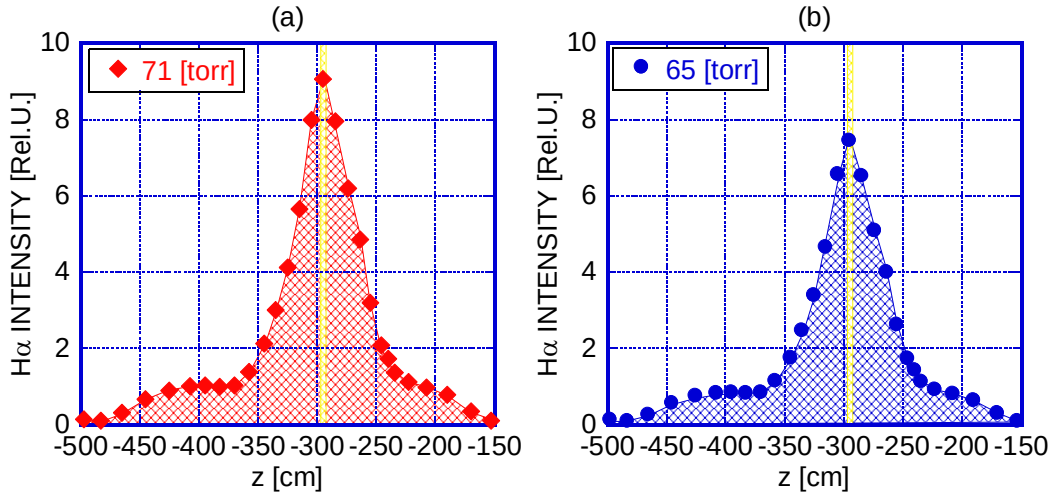

Fig. 4.13　z axis distribution of generated particle on the plenum pressure.

Chapter 5 Neutral particle behavior in the SMBI experiments

The proper control of gas fueling is very important for obtaining high-density plasmas that perform well. Control of fueling enables optimization of the core-plasma density, which leads to fewer neutral particles dispersed in the peripheral area. In the magnetic confining device, the role of fueling device is to supply fuel particles and to control the plasma density profile. Two major fueling methods have been used in the plasma experiments. One is the gas puffer that is a conventional method and has been used the early period of the fusion plasma study. The other is the ice-pellet injection that can effectively increase the density in the plasma core region. However the pellet system is complicated compared with the gas puffer system. Supersonic Molecular beam injection (SMBI) has been developed as a new method that can combine both advantages of the pellet injection and the conventional gas puffer, i.e., simpleness of the device, high fueling efficiency, and rapid response [55, 56]. Furthermore the pellet system is not so much for the small devices in the confining device because its system is complicated. In addition, it is not easy to make a pellet small enough to control the core-plasma density in small devices. SMBI provides high-speed and high-directive gas injection by using a plenum pressure higher than what is used in conventional gas puffing, so that neutral particles can be injected deeper into the core plasma. SMBI has been successfully applied to some devices [57, 58] and is considered especially effective for small and relatively low-density devices such as GAMMA 10.

In GAMMA 10, SMBI has been installed at the central cell. The central cell has a simple solenoidal magnetic configuration that uses ten pancake coils. In addition, the central cell has many observation ports for observing the central cell plasma. High-speed camera has been also installed at the central cell mid-plane for measuring the plasma behavior. The first experimental results of SMBI showed that, compared with conventional gas puffing, this technique leads to higher-density plasmas at the core region.

The neutral particle behavior was investigated based on 2-dimentional image captured by high-speed camera. Furthermore, the neutral transport simulation was also employed for investigating the spatial profile, such as radial distribution of hydrogen atom and molecule. These results enable us to understand the penetration depth. Calculated distribution of hydrogen atom and molecule is transformed to Hα line emission based on CR model in order to compare between the experimental results and simulation results. The purpose of this study is to investigate, both experimental and simulation, the characteristic of neutral particles during SMBI. One of the differences between the conventional gas puffer and SMBI is plenum pressure. Therefore we investigated how SMBI depends on the plenum pressure. In addition, by using two nozzles, the effects on the neutral particle behavior are also investigated. In this study, the main issue is to investigate neutral particle behavior from SMBI.

5.1 Experimental set up

Figure 5.1 shows a cross-section of the GAMMA 10 central-cell, a layout of the SMBI system, and the objective optical system for the high-speed camera. A high-speed camera is installed at central-cell to observe the plasma near the central limiter. The high-speed camera observes the two-dimensional (2-D; i.e., x-z, or y-z) response of the plasma to SMBI and is sufficiently capable of measuring visible-light emission. By using dual blanch optical fiber bundles, the camera system has a line of sight in the horizontal direction and one in the vertical direction of the plasma cross-section. The expansion of the molecular beam injected by SMBI in the axial (z) direction and its penetration depth into the plasma can be estimated from the 2-D image in two directions. The SMBI system consists of a fast solenoid valve with a magnetic shield. The plenum pressure is usually 1 MPa and the pulse width is 0.5 to 1.0 ms. In this study SMBI system, two type of nozzle was used in combination with the solenoid valve. One is the straight nozzle. The shape of the straight nozzle is simple cylindrical form, and it is made of SUS316. The other is the Laval nozzle. That nozzle is most widely used design in modern aerospace and rocketry applications. That nozzle has three sections, one is the inlet section, another section is throat section, and the other is exhaust expansion section. The characteristic of Laval nozzle is that the temperature and pressure of gas decreasing as Mach number of exhaust gas increasing. Figure 5.2 shows that the configuration of the Laval nozzle.

5.2 Typical experimental results

We carried out the SMBI experiments in three conditions, one condition is without nozzle, another condition is with straight nozzle, and the other condition is with Laval nozzle. Figure 5.3 shows a picture at the bottom of the central cell in the vacuum chamber on each experimental condition. SMBI pulse was injected to typical plasma heated by ICRF only. Figure 5.4 shows time behavior of diamagnetism and electron line density. Electron line density considerably increased just after SMBI injection, however the diamagnetism decreased. Figure 5.5 shows a typical 2-D image captured by the high-speed camera of visible emission during SMBI from the GAMMA 10 plasma. The time behavior of 2-D images is shown in Fig. 5.5.

5.3 Analysis method in the experimental results

To investigate the directivity of the molecular beam injected by SMBI, we investigated the axial profile of the neutral transport by using the 2-D vertical-direction image. The figure 5.6 shows the

peak emission intensity of 2-D image captured by high-speed camera. The left side of Fig. 5.6 shows the intensity emitted in the horizontal direction; the right side shows that emitted in the vertical direction. We also investigated the distribution of emission intensity at the broken line on the right side of Fig. 5.6 (the broken line was drawn over the SMBI injection port). Figure 5.7 shows the distribution of emission intensity at the broken line as obtained from the 2-D image in Fig. 5.6. We used the full width at half maximum (FWHM) of the distribution emission intensity in Fig.5.7 as an index of the axial neutral transport. Because the intensity profile generally does not change as the intensity increase, the best signal-to-noise ratio is obtained at the peak intensity. Thus, this timing is appropriate for obtaining the distribution of emission intensity. We analyzed the FWHM for each SMBI plenum pressure on each experimental condition with/without nozzle. Figure 5.8 shows how the FWHM depends on the plenum pressure. As shown in Fig.5.8, the FWHM value decreases with increasing SMBI plenum pressure.

As shown in Fig. 5.8, the FWHM value with the straight nozzle is lower than the case without nozzle on all plenum pressure. Furthermore the FWHM is lower than the diameter of the plasma. This means that the effect of the straight nozzle reduced the diffusion of the neutral particles from SMBI in the peripheral region. In both cases, the FWHM value decreases with increasing the SMBI plenum pressure in the range of the lower plenum pressure ($\leq$ 1 MPa). However, the value of FWHM does not decrease with increasing the plenum pressure in 1 MPa or higher in the case using the straight nozzle. This means that the directivity of particle was suppressed by the collision between neutral particles through the straight nozzle in the case of higher plenum pressure. In addition, in the case with Laval nozzle, only one data was plotted on the Fig5.8. This result was the lowest value of the FWHM. Unfortunately, the accident was happened. The Laval nozzle was broken. Therefore we could not obtain more data. However the effect of Laval nozzle was observed in this data.

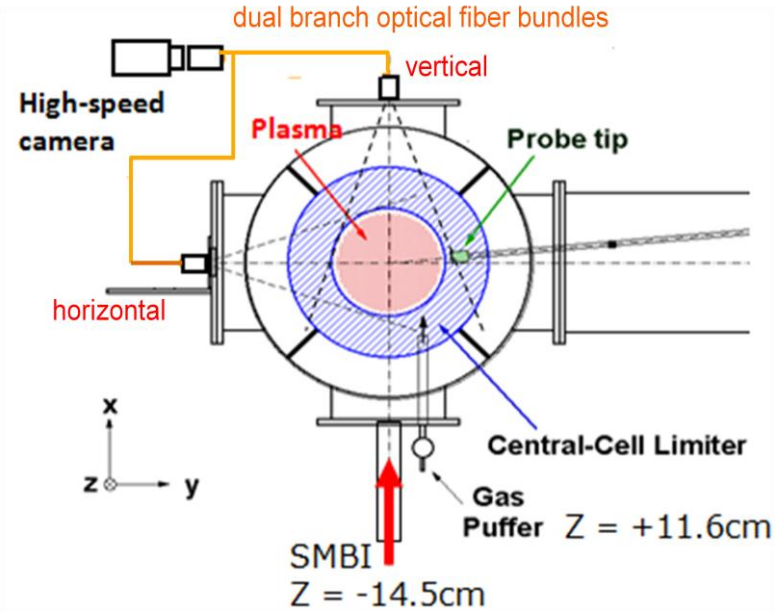

Fig. 5.1 Cross-section of the central cell and locations of SMBI and high-speed camera.

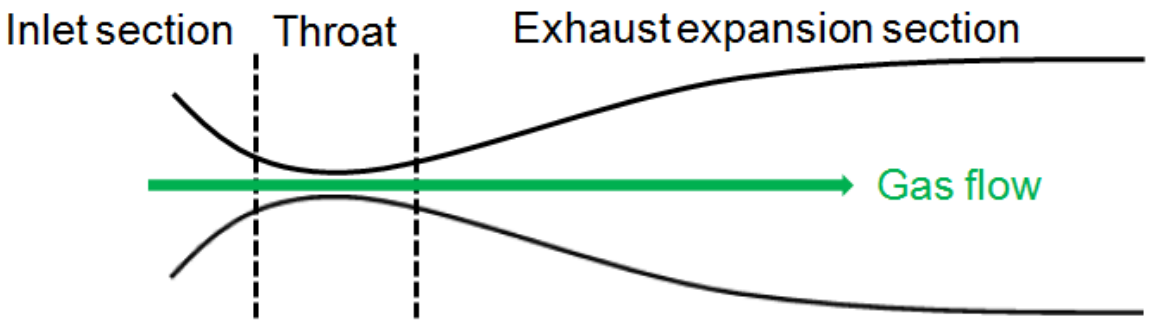

Fig. 5.2　Schematic view of Laval nozzle

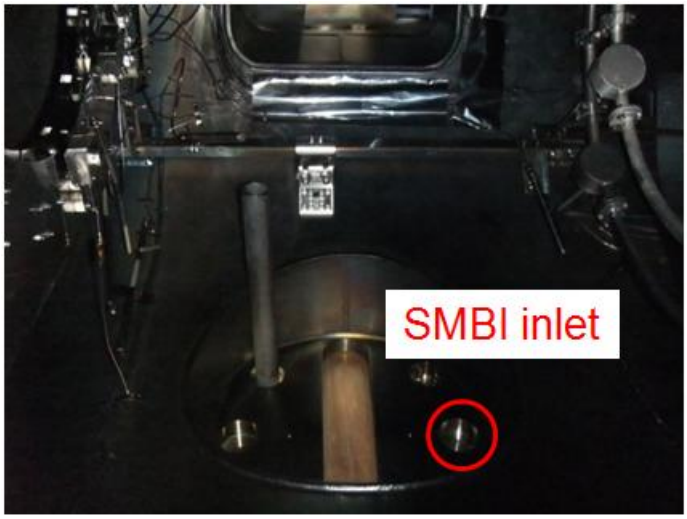

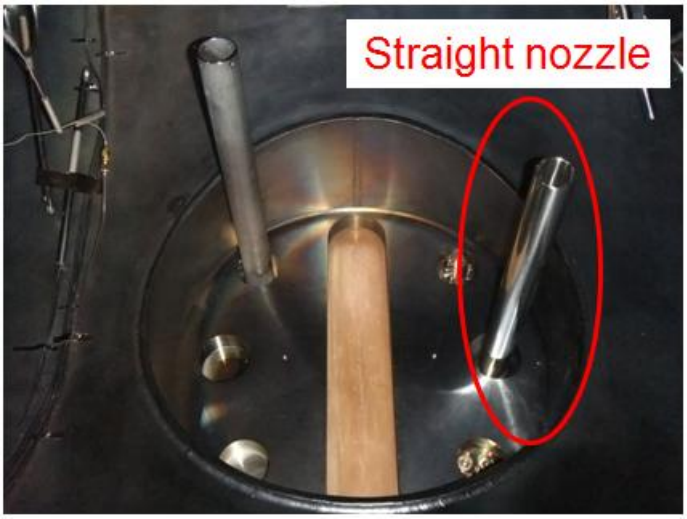

Fig. 5.3 the bottom of the central cell near the SMBI inlet in three experimental conditions.

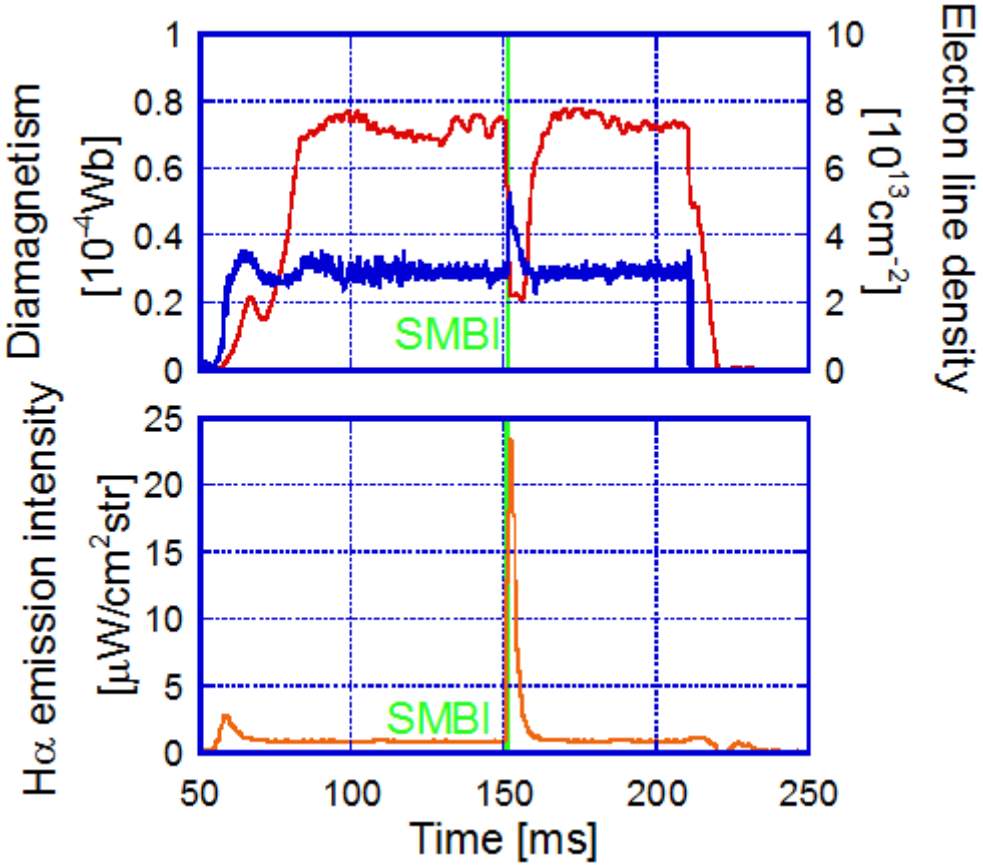

Fig 5.4　Time behavior of plasma parameter.

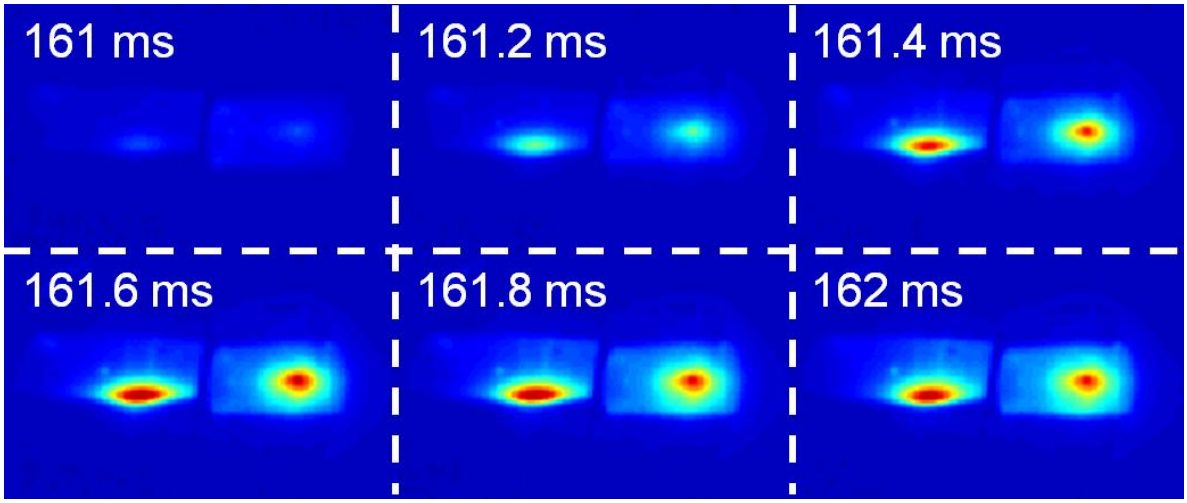

Fig 5.5　Time behavior of 2-D images.

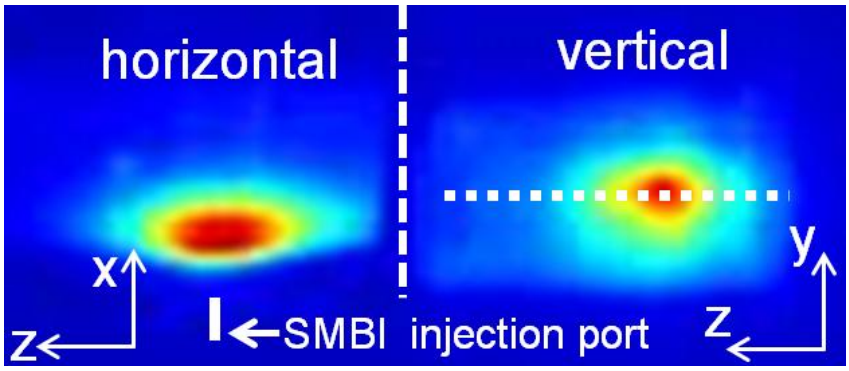

Fig 5.6　The peak emission intensity of 2-D image

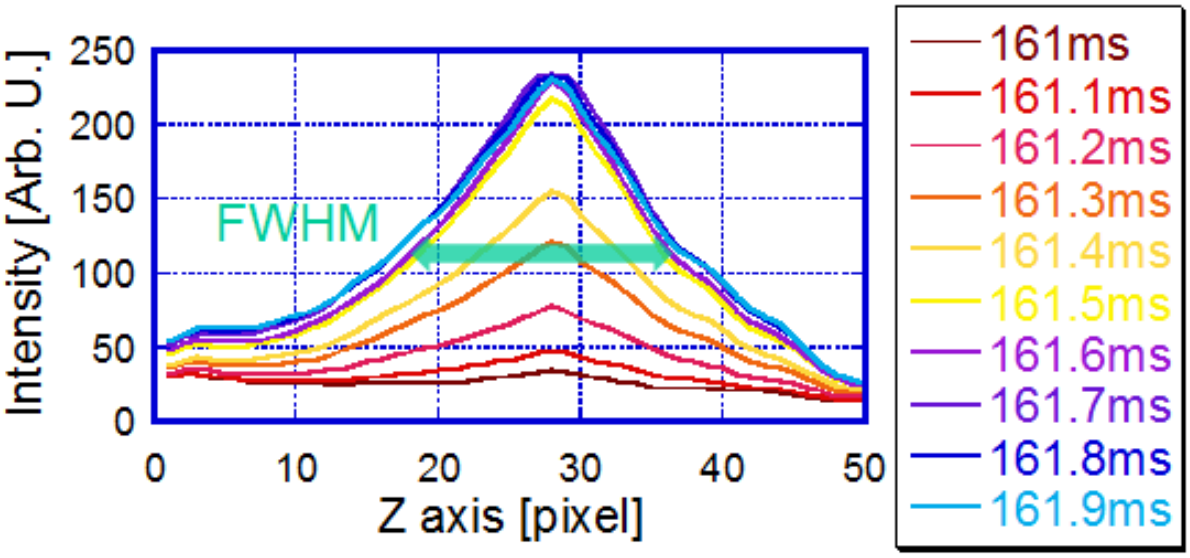

Fig 5.7　Distribution of emission intensity at the broken line as obtained from the 2-D image in Fig. 5.6.

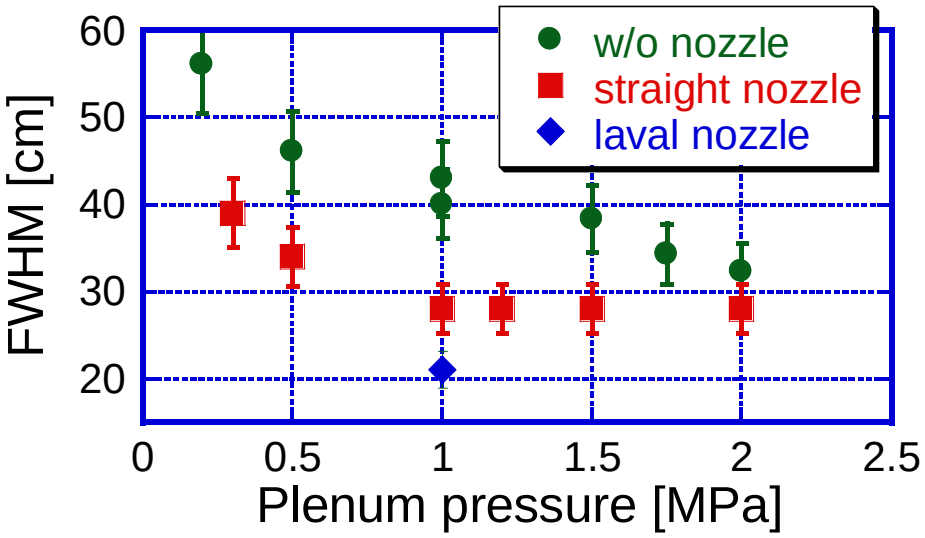

Fig 5.8　Dependence of FWHM on the plenum pressure.

5.4 Simulation analysis of new gas fueling method

5.4.1 Improvement of the mesh model for neutral transport in SMBI experiments

In this section, neutral behavior from SMBI was investigated by using the Monte-Carlo simulation. Figure 5.9 shows the fully 3-D mesh model applied to the central cell for the simulation. In this mesh model, the limiters and antennae of the ICRF are precisely implemented in a realistic configuration. Furthermore this mesh model was improved for modeling SMBI experiments; it was expanded around the SMBI injection port and new mesh was added in a realistic configuration about the SMBI valve, straight nozzle. Laval nozzle geometry is considerably complicated. Therefore the experimental condition of the Laval nozzle is only reproduced the initial condition of the test particle. The schematic view of the vicinity of the straight nozzle was also shown in Fig. 5.9. The background plasma parameters ($T_e \approx 40$ eV, $T_i \approx 5$ keV, $n_e = n_i \approx 2.0\times10^{12}$ cm^{-3}, *etc*) on each mesh were determined based on the experimental data, as shown in Fig. 5.10. The axial distribution of Hα emission was calculated to investigate the neutral transport during SMBI.

5.4.2 Initial condition of test particles

Here we have to discuss the initial particle condition of particle. In the DEGAS simulation in GAMMA 10, neutral source is given in a cosine distribution. However the neutral source from SMBI makes different profile from the conventional process such as gas puffer and recycling phenomena according to the experimental results. Hence, the neutral source is modified for the neutral source due to the SMBI. To simulate the molecular beam injected by SMBI, we introduce σ_{div} to index the divergence angle of the initial particles. If the angular profile of launched particles has a cosine distribution, the divergence-angle index is $\sigma_{div} = 1$. If $\sigma_{div} = 0.5$, for example, the horizontal component of the velocity vector in the cosine distribution is reduced to half. Figure 5.11 shows a schematic of the distribution of launched particles for $\sigma_{div} = 1$, $\sigma_{div} = 0.5$ and $\sigma_{div} = 0.33$. We clarified that the experimental result for conventional gas puff was reproduced under the conditions $\sigma_{div} = 1$[48]. We also investigate the way in which the axial distribution of Hα emission depends on σ_{div}.

5.4.3 Axial distribution of Hα line emission intensity

Figure 5.12 shows the axial distribution of the Hα emission near the SMBI injection port, as calculated by DEGAS and for three cases of divergence-angle index. As same as experimental results analysis, we used the FWHM of the axial distribution of emission intensity calculated by

DEGAS as an index of the axial neutral transport.

5.4.4 Comparison of the experimental results

The axial distribution of the experimental results and simulation results was compared, as shown in Fig.5.13. Figure shows the simulation results for $\sigma_{div} = 1$ does not agree with the emission FWHM obtained from the experimental results. The simulated and experimental results are compared in Fig.5.13. The hatched zone in Fig. 5.13 shows the FWHM obtained from the experimental results. As shown in Fig. 5.13, the SMBI must be modeled under the initial particle conditions of $\sigma_{div} = 0.5$ reproduce the experimental results for a plenum pressure between 0.2 and 2.0 MPa. These results suggest that a difference exists between SMBI and conventional gas puff with regard to the initial conditions of the divergence angle of the initial particles.

5.5 Analysis of Spatial Distribution of Neutral Particles

In the case that the initial condition was selected based on the experimental results, the experimental results was reproduced in the simulation. We carried out the simulation in three conditions. One condition is the configuration of SMBI with naked valve and $\sigma_{div} = 0.5$ (case 1), another is the configuration of SMBI with straight nozzle and $\sigma_{div} = 0.5$ (case 2), the other is the condition of SMBI with the Laval nozzle and $\sigma_{div} = 0.25$ (case 3). Figure 5.16 shows the schematic view of the three simulation conditions of the mesh model. Figure 5.17 shows the simulation results of the Hα emissivity on plasma cross-section. In the case 1, amount of neutral particle diffused in peripheral region. In the case 2, the distribution of the neutral particle on the cross-section was more convergence than that of case 1. In the case 3, neutral particle was localized at the bottom of plasma. In addition, diffusion of neutral particle to the peripheral region was suppressed. These simulation results indicated that the neutral particle density was controlled by the directivity of the injected particles. In the next step, by using this result, the spatial structure was discussed in order to evaluate the penetration depth. It is the very important key for the supply into the core region to understand what decides the penetration depth. In this study, the penetration depth was evaluated based on the peak position of axial distribution from the edge to the core of plasma on the cross-section. Figure 5.15 shows the analysis method for the penetration depth. Here, we introduce λ_{pnt} to the index of the penetration depth.

5.5.1 Dependence of the penetration depth on divergence angel

At first, the dependence of the penetration depth on the divergence angle was investigated. The penetration depth was investigated in three simulation conditions showed in Fig. 5.16. Figure 5.18 shows the comparison of the penetration depth. However it was not confirmed that the penetration depth depended on the divergence angle. The distance to the plasma and divergence angle did not affect the penetration depth.

5.5.2 Dependence on the radial electron temperature profile

As described in the previous subsection, the distance to the plasma and the divergence angle did not affect the penetration depth. The lifetime of the neutral particles in a fusion device are a function of their velocities and the mean free path length of interaction with plasma. Assuming the ion density is equal to the electron density, the mean free path length is a function of the electron density ne, the reaction rates of the charge exchange $< \sigma v >_{CX}$ and electron impact ionization $< \sigma v >^{e}_{ion}$ as follows,

$$\lambda_p = \frac{v}{n_e(< \sigma v >^{e}_{ion} + < \sigma v >_{CX})}, \tag{5.1}$$

where ν is the velocity of the neutral particles. Considering a function of the mean free path length, the reaction rate depends on the electron temperature. It has been reported that SMBI has an additional effect of plasma edge cooling [58]. Therefore we carried out the simulation in different electron profile.

Figure 5.19 shows the electron temperature profile used in this simulation. The simulation was carried out in the four different electron profiles in order to investigate the spatial distribution. The distribution of the Hα emissivity on the plasma cross-section was showed in Fig. 5.20. As shown in the figure 5.20, neutral particle ionized in peripheral region was decreased in the case that electron temperature was low. However the difference of the directivity of neutral particles was not observed in four cases. On the basis of this result, we evaluate the penetration depth. Figure 5.21 shows the simulation results of the penetration depth. As the electron temperature in peripheral region decreases more, the penetration depth becomes longer. This result indicates that radial electron profile significantly influences the penetration depth. In other word, plasma edge cooling of another effect of SMBI is a key point of clarifying the mechanism of penetration depth.

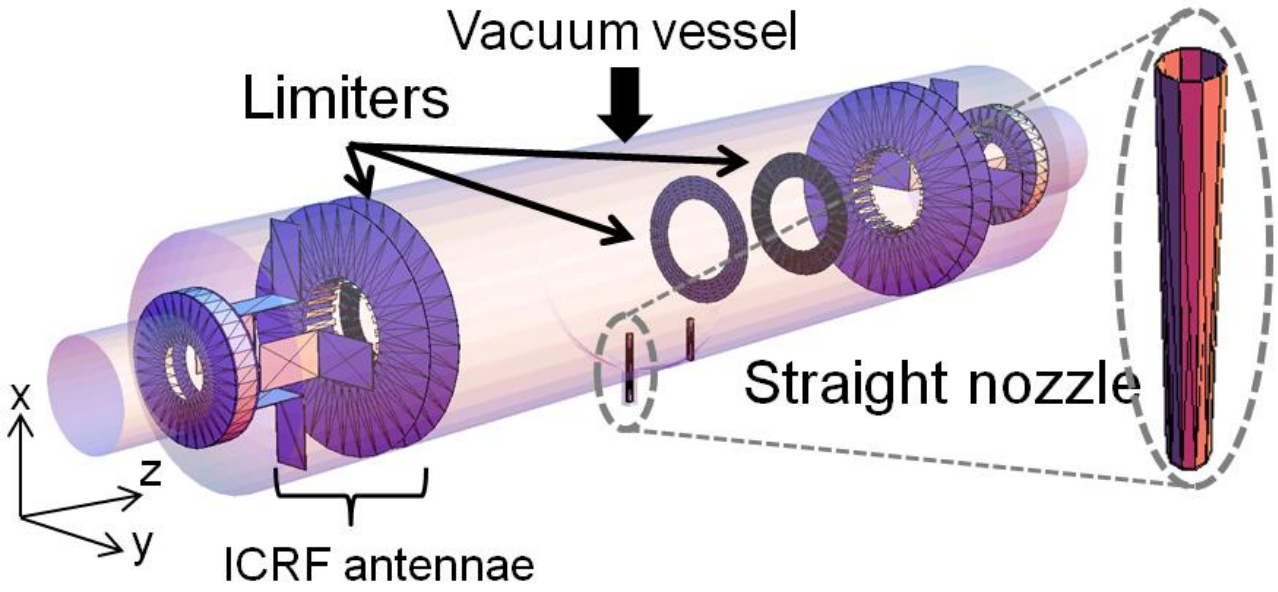

Fig. 5.9　Fully 3-D mesh model applied to the central cell.

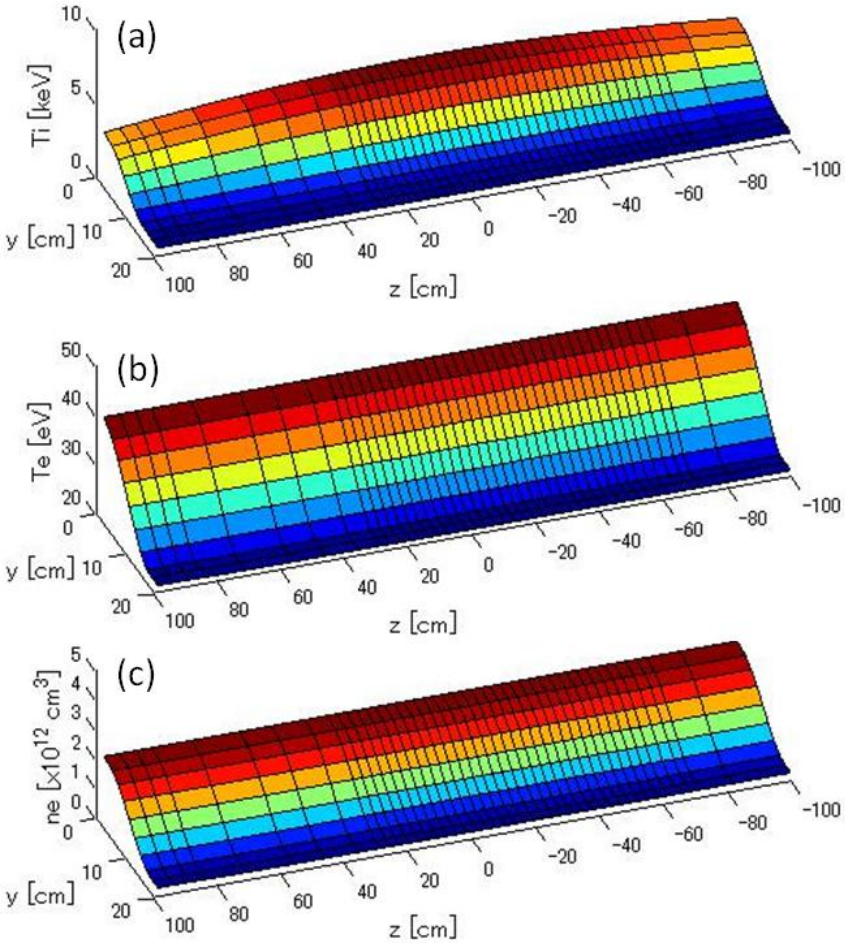

Fig.5.10　Input plasma parameters applied to DEGAS simulation.
(a) ion temperature, (b) electron temperature,
(c) electron density.

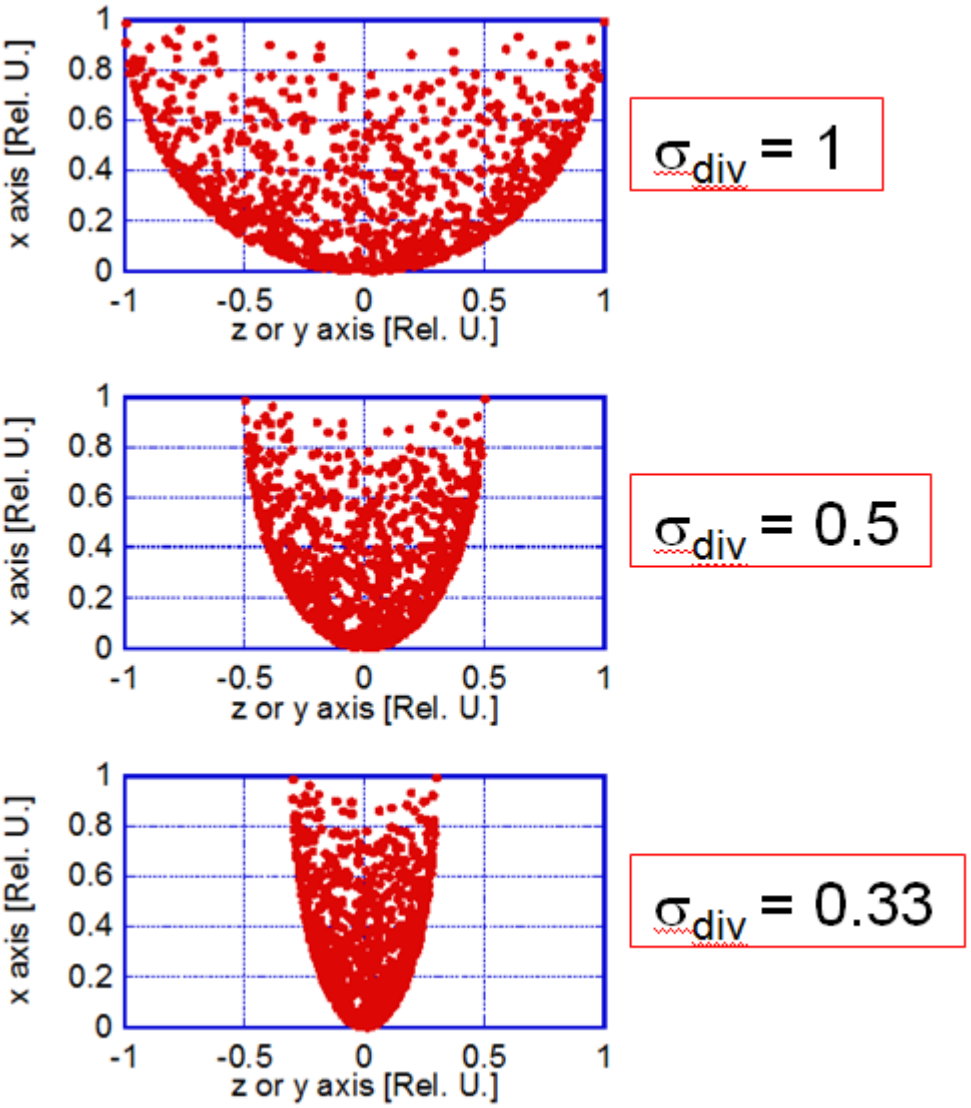

Fig 5.11　Initial condition of test particles. (σ_{div} = 1 : cosine distribution)

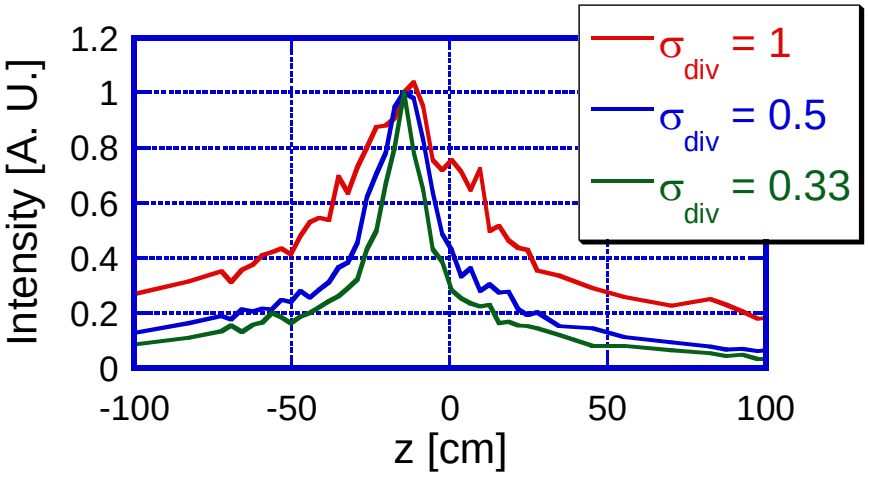

Fig 5.12　Distribution of Hα emission intensity in three conditions.

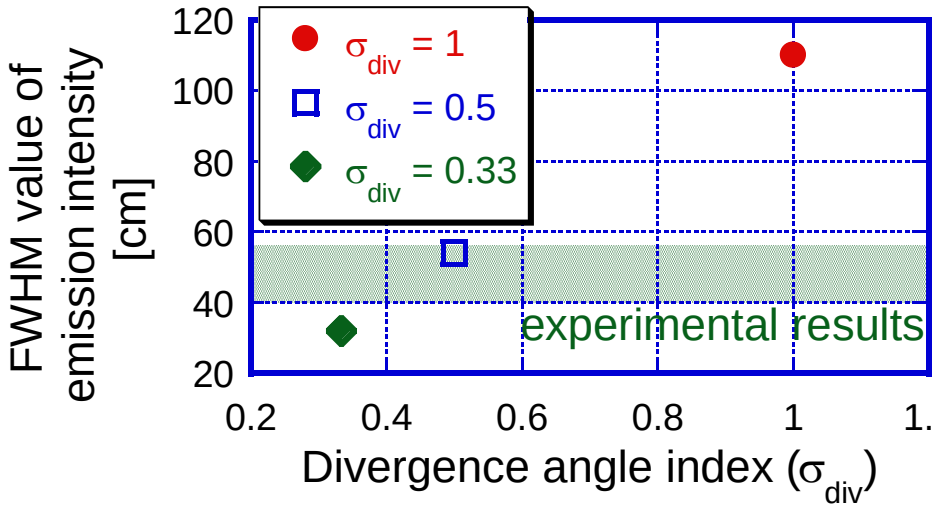

Fig 5.13　Comparison of FWHM between experimental results and simulation results calculated in three conditions.

(a)

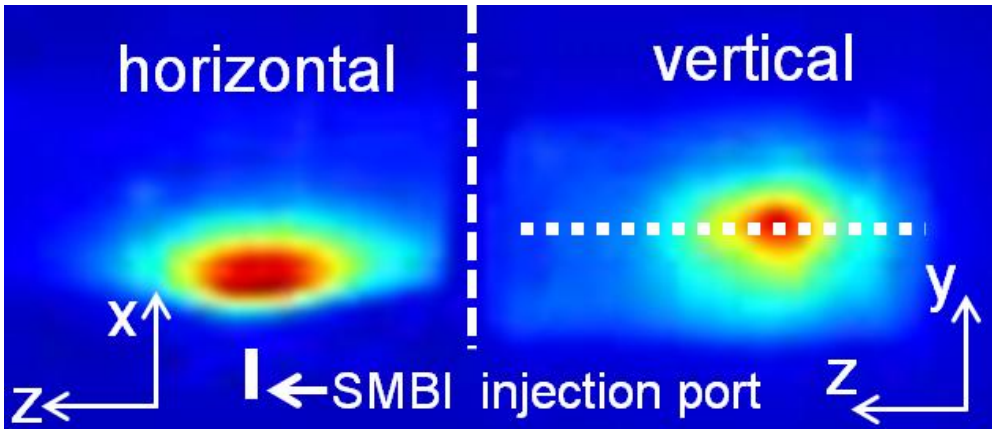

(b)

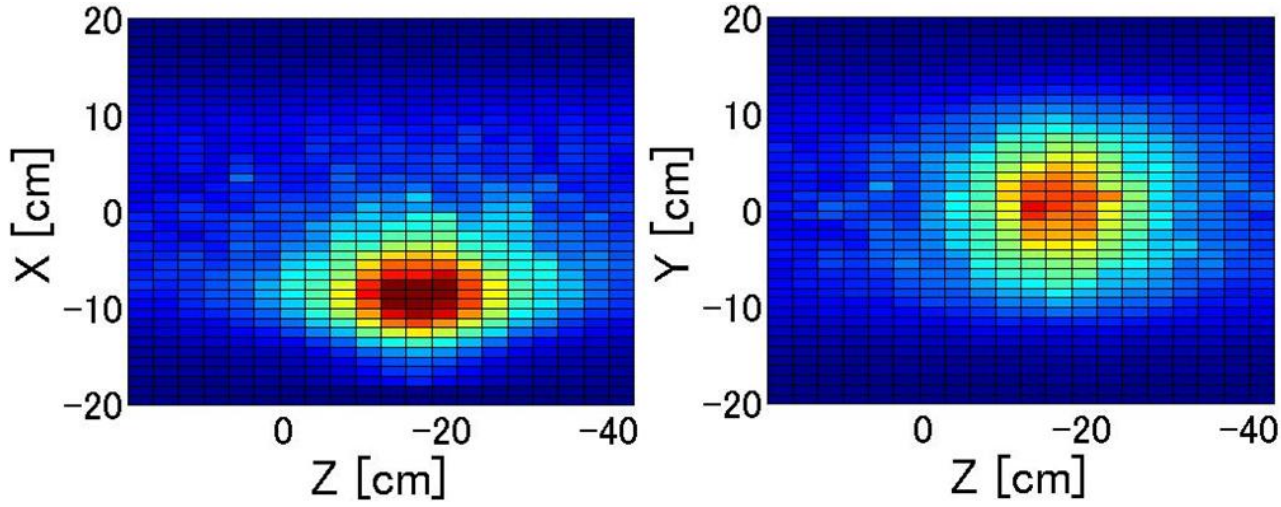

Fig. 5.14 Comparison between (a) 2-D image captured by high-speed camera and (b) simulation results.

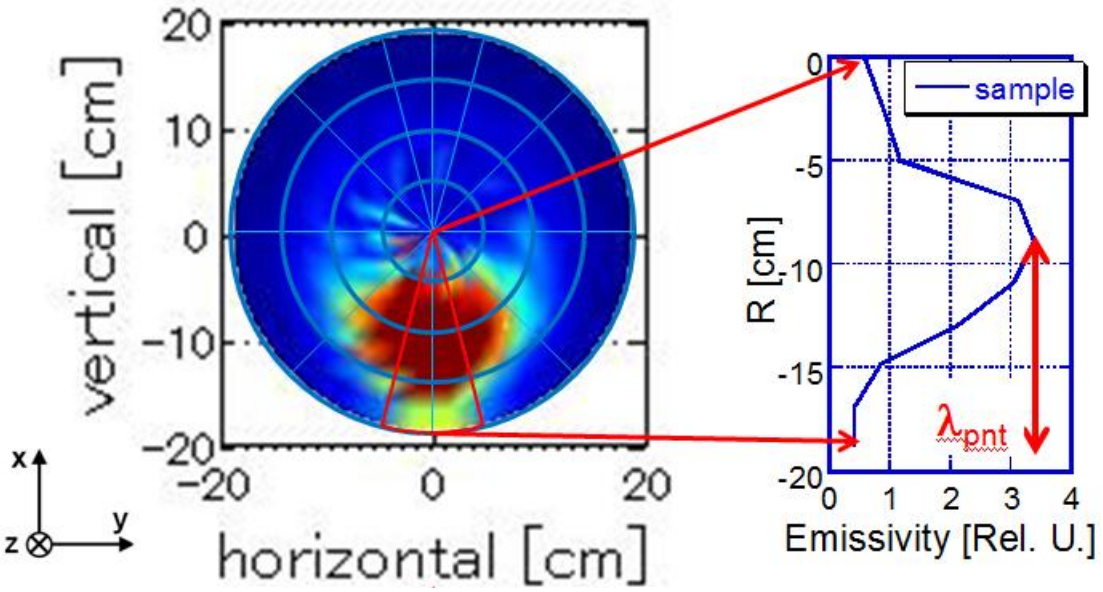

Fig. 5.15 Analysis method for the penetration depth.

Case 1, only valve (without nozzle)
σ_{div} = 0.5

Case 2, with straight nozzle
σ_{div} = 0.5

Case 3, with laval nozzle
σ_{div} = 0.25

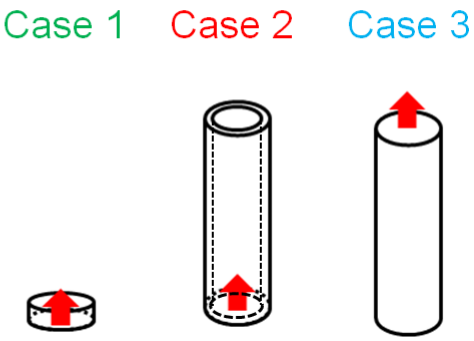

Figure 5.16 Schematic view of the three simulation conditions of the mesh model.

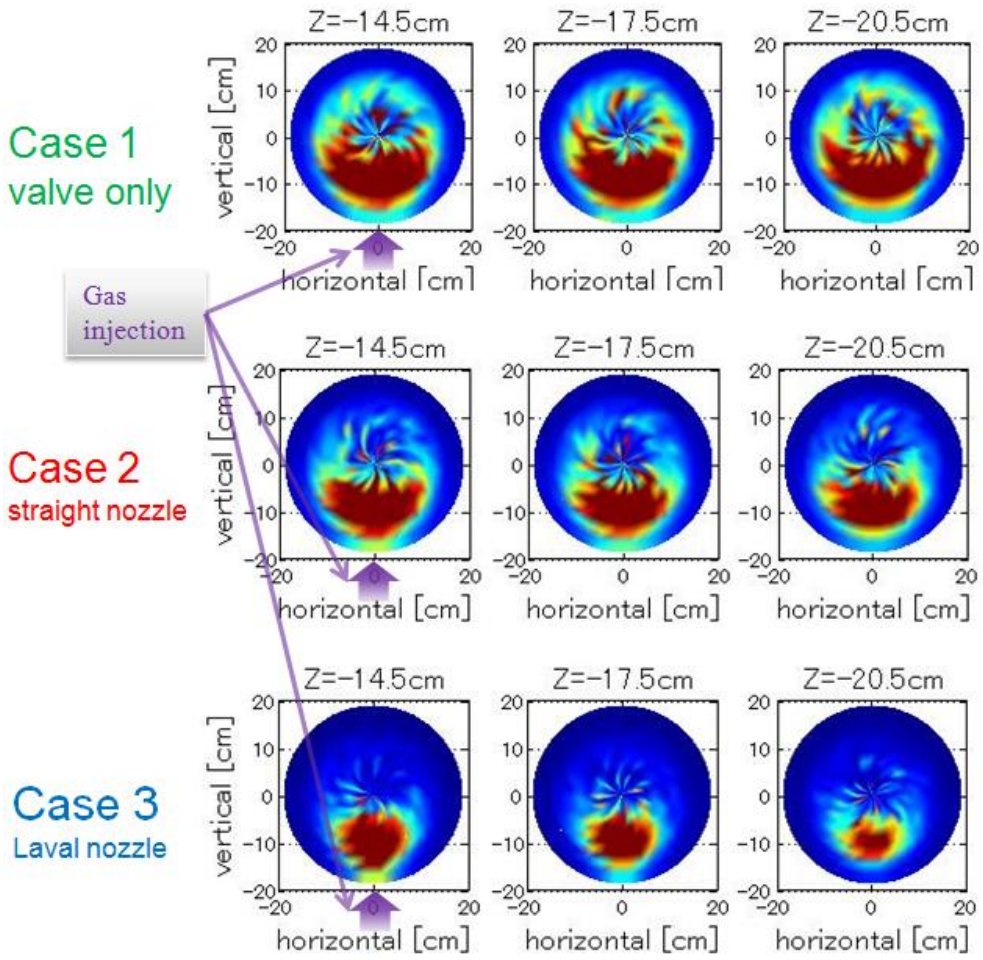

Fig. 5.17　Hα emissivity on the plasma cross-section under three different conditions.

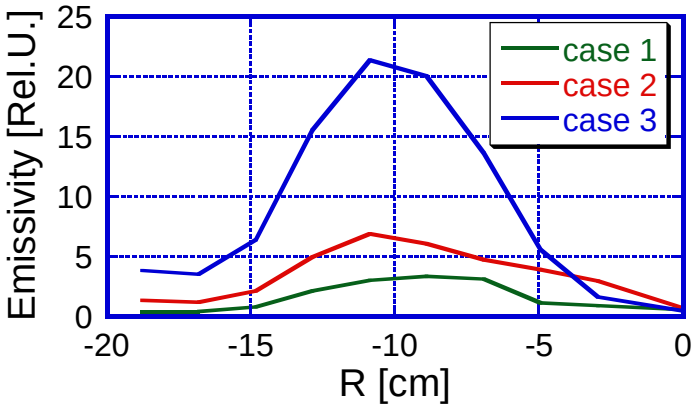

Fig. 5.18 Dependence of the penetration depth on the divergence angle and valve configuration.

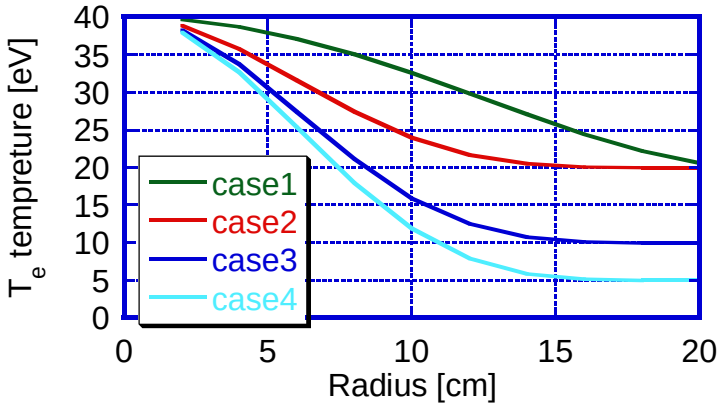

Fig 5.19 Electron temperature profile of the initial condition.

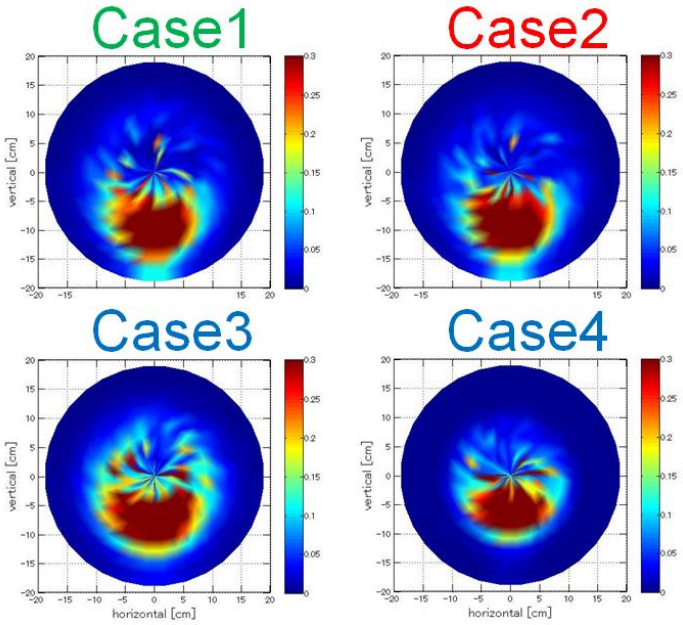

Fig. 5.20　Hα emissivity on the plasma cross-section under the four cases of T_e profile

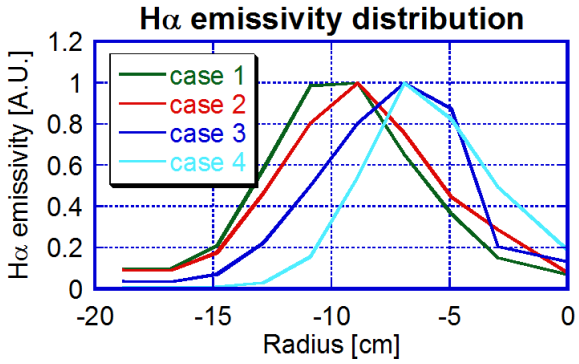

Fig 5.21　Evaluation of the penetration depth in four cases of radial electron profile.

Chapter 6 Conclusion

In this thesis, we studied the influence of various kinds of particle sources on the neutral particle behavior in the GAMMA 10 tandem mirror plasmas. In the C-ECRH experiments, the effect of neutral particle on the plasma sustainment was investigated from the viewpoint of particle balance for optimizing the experimental condition. In the SMBI experiments, neutral particle behavior caused by SMBI as new particle supply method was investigated in order to clarify the difference of neutral particle behavior between the conventional gas puffer and SMBI. We employed the fully three-dimensional Monte-Carlo simulation code (DEGAS ver.63) in order to understand the spatial distribution of neutral particles. New mesh model for each experimental configuration was constructed and applied to the GAMMA 10 central cell. We successfully performed the neutral particle simulation by using new mesh model. The contents of thesis were summarized as follows.

6.1 Particle control based on the particle balance in the C-ECRH Experiments

It was occasionally observed that the loss particle is enhanced by C-ECRH injection. It is speculated that the degradation of the plasma parameters during C-ECRH injection was caused by the loss particle. In the experiments, the difference of the experimental condition between the cases of plasma sustainment and collapse was investigated from Hα line measurements. The experimental optimization from the viewpoint of the particle balance shows that the increase of limiter recycling source, ICRF power and the throughput of gas puff prevent plasma collapse.

The optimized condition of the ECRH experiments was also investigated by using the DEGAS simulation. In order to make a precise evaluation of the ionization rate in the whole central cell, the mesh model of the simulation was improved. From the simulation results, the difference of generated particles in the central cell between the cases of plasma sustainment and collapse was estimated to be around 10 %. It is found that the around 10 % difference of total plasma production rate gives a substantial effect on the plasma sustainment.

6.2 Neutral particle behavior in the SMBI Experiments

From the measurement of the 2-dimentioanl image captured by high-speed camera, it is clarified

that the directivity of neutral particle from SMBI depends on the plenum pressure from the measurement of. By using various kinds of nozzles, the diffusion of the neutral particle in the plasma perihelia could be suppressed. However FWHM of axial distribution of the Hα emission was saturated in the higher plenum pressure in the case of the straight nozzle.

The neutral transport simulation was successfully applied to the SMBI experiment for the first time. The simulation results roughly reproduced the experimental results in the case of proper initial condition. This result will enable us to discuss the spatial structure for investigating the effect of the directivity and the penetration depth in the plasma column. Cross-sectional view of Hα emission can be evaluated by using the DEGAS simulation during SMBI. The directivity considerably affects the distribution of the Hα emissivity. This indicates that the neutral density in the plasma and the peripheral region could be controlled by the directivity of the injected particle. We also evaluated the penetration depth of SMBI-induced particles and it is clarified that the penetration depth has no dependence on the directivity of the particles from the radial distribution of Hα emissivity in the plasma cross-section.

The simulation was carried out in the different profiles of electron temperature in order to take into account of the plasma edge cooling effect due to SMBI. The simulation results indicated that the penetration depth depended on the distribution of the edge electron temperature. Therefore plasma edge cooling of another effect of SMBI is another key point of clarifying the mechanism of penetration the neutral particles.

6.3 Concluding Remark

From the above experimental and simulation results, plasma particle generation in the whole area of the system can be evaluated by using the DEGAS code under the condition of the different particle sources (gas puffing source or recycling source). Furthermore, the effect of the difference of total ionized particles on the plasma performance can be evaluated quantitatively. The above results indicate that the neutral particle simulation is a useful tool for the particle balance analysis in order to optimize the experimental condition. In addition, not only the behavior of neutral particles from the conventional gas puffer, but also that from SMBI can be reproduced for the first time. These results enable us to analyze in detail the neutral particle behavior without dependence of the plasma configuration and of the machine structure. The beneficial knowledge obtained from this thesis also contributes to the analysis of the neutral transport in the case of the complicated magnetic configuration, such as torus devices and helical devices.

Acknowledgments

The author would like to expresses his sincere gratitude to Prof. Y. Nakashima at University of Tsukuba for his continuous guidance and encouragement in the course of the present study. His helpful suggestion and significant discussion are essential for the accomplishment of the present study.

He wishes to thank to Prof. M. Ichimura and Prof. T. Imai for their continuing interest in the present study. He also wishes to thank to Prof. M. Sakamoto, Prof T. Kariya and Prof. M. Yoshikawa for helpful advice.

He would like to deeply appreciate Dr. S. Kobayashi at Kyoto University for his kind assistance on the neutral transport. He also would like to deeply appreciate Prof. N. Nishino at Hiroshima University.

He would like to thank to Prof. M. Shoji at National Institute for Fusion Science for significant support on the DEGAS calculations.

He wishes to thank to Dr. A. Murakami at National Institute for Fusion Science.

This study is partly supported by the bi-directional collaboration research program of National Institute for Fusion Science, Kyushu University and University of Tsukuba.

Finally he would like to thank the members of GAMMA 10 groups for their collaboration in the experiments and for helpful discussions.

Appendix

DEGAS Code

The computational process for the neutral density and temperature in plasma is described in this appendix.

A.1 Boltzmann Equation

The lifetimes of the neutral particles in a fusion device are a function of their velocities, the mean free path length of interaction with the plasma λ_p and the distances to the device walls l_ω. Assuming the ion density is equal to the electron, the mean free path length is a function of the electron density n_e, the reaction rates of the charge exchange $<\sigma v>_{CX}$ and electron impact ionization $<\sigma v>_{ion}^{e}$ as follows,

$$\lambda_p = \frac{v}{n_e(<\sigma v>_{ion}^{e} + <\sigma v>_{CX})} \tag{A.1}$$

where v is the velocity of the neutral particles. Then mean free path length of the particles, l_{tot} is

$$l_{tot} = \frac{\lambda_p l_\omega}{\lambda_p + l_\omega} \tag{A.2}$$

In order to obtain the neutral density and temperature in a plasma, it is assumed that the Boltzmann equation describing the neutral particle distribution $f(\mathrm{x},\mathrm{v})$ over position x, and velocity v, space is time-independent,

$$v \cdot \nabla f(\mathrm{x}) = C(f)(\mathrm{x},\mathrm{v}) \tag{A.3}$$

where $C(f)$ is the neutral-plasma collision term. For simplicity, assuming that the plasma is a slab bounded on one side by a flat wall, Eq. A.3 can be rewritten in only 1-dimension,

$$v_x \frac{\partial f}{\partial x} = C(f) \tag{A.4}$$

for $x > 0$, with one boundary condition on f, at the wall at $x = 0$,

$$f(0, v) = f_+(v) \tag{A.5}$$

In the collision term for atomic hydrogen, the electron impact ionization and charge exchange processes were included. Then the ionization term $S(f)$ in $C(f)$ is,

$$S(f) = -f(x, \mathrm{v}) \int_{\omega} \|\mathrm{v} - \mathrm{w}\| \sigma_e f_e(x, \mathrm{w}) d\mathrm{w} \tag{A.6}$$

where $f_e(x,\mathrm{w})$ is the electron distribution function and $\|\mathrm{a}\|$ denotes the length of the vector a. Now in general $\|\mathrm{w}\| \gg \|\mathrm{v}\|$, so that, assuming $f_e(x, \mathrm{w}) = n_e(x) f_M(\mathrm{w})$, where f_M is a Maxwellian velocity distribution, Eq. A.6 can be rewritten as,

$$\begin{aligned} S(f)(x, \mathrm{v}) &= -f(x, \mathrm{v}) n_e(x) \int_{\omega} \|\mathrm{w}\| \sigma_e f_M(\mathrm{w}) d\mathrm{w} \\ &= -f(x, \mathrm{v}) n_e(x)_S \end{aligned} \tag{A.7}$$

where

$$s = \int_{\omega} \|\mathrm{w}\| \sigma_e f_M(\mathrm{w}) d\mathrm{w} \tag{A.8}$$

The charge exchange term, $X(f)$ in $C(f)$ is,

$$X(f)(x, \mathrm{v}) = \int \|\mathrm{v} - \mathrm{w}\| \sigma_{CX} [f(x, \mathrm{w}) f_i(x, \mathrm{v}) - f(x, \mathrm{v}) f_i(x, \mathrm{w})] d\mathrm{w} \tag{A.9}$$

Simplifying Eq. A.9 is the fact that $\sigma_{CX}\|\mathrm{v} - \mathrm{w}\|$ is a slowly varying function of the relative velocity, which can then be assumed to be a constant c. Taking$f_i(x, \mathrm{v}) = n_i(x) f_M(\mathrm{v})$, Eq. A.9 then becomes

$$X(f)(x, \mathrm{v}) = n_i(x) c \left[f_M(\mathrm{v}) \int_{\omega} f(x, \mathrm{w}) d\mathrm{w} - f(x, \mathrm{v}) \right] \tag{A.10}$$

Returning to Eq. A.3, assuming $n_e = n_i = n$, the following relation can be observed,

$$
\begin{aligned}
v_x \frac{\partial f}{\partial x} &= S(f) + X(f) \\
&= -fns + cn\left[f_M \int_{\omega} f(x, \mathrm{w}) d\mathrm{w} - f\right] \\
&= -fn(s+c) + ncf_M \int_{\omega} f(x, \mathrm{w}) d\mathrm{w}
\end{aligned}
\tag{A.11}
$$

It is useful to parameterize the distance variable to units, z of mean free path lengths (the optical depth),

$$
z(x) = \int_0^x \frac{dy}{\lambda_{tot}(y)} = \int_{\omega}^x \frac{n(y)(c+s)dy}{v_{T_i}} \tag{A.12}
$$

where v_{T_i} is the ion thermal velocity. With this change of variables, integrating Eq. A.11 over v_y and v_z gives,

$$
u \frac{\partial F}{\partial z} + F(u,z) = \frac{c}{s+c} g(u) \int_{-\infty}^{\infty} F(u,z) du \tag{A.13}
$$

where $u = v_y / v_{T_i}$, $F(u,z) = \iint f(x,v) dv_y d\, v_z$, and $g(u)$ is the ion velocity distribution.

To illustrate how the Monte Carlo method can be used to solve Eq. A.3, simplify Eq. A.3, for argument's sake, by assuming that no charge exchange occurs, so that the 1-dimensional version [Eq. A.13] of Eq. A.3 is

$$
u \frac{\partial F}{\partial z} = -F(u,z) \tag{A.14}
$$

Making the further assumption that $|u| = 1$, Eq. A.14 has the solution

$$
\begin{aligned}
\mathrm{F(x)} &= \exp[-\mathrm{z(x)}] \\
&= exp\left[-\int_0^x \frac{d_y}{\lambda_{tot}(y)}\right]
\end{aligned}
\tag{A.15}
$$

Now the solution Eq. A.14 can be derived from a different point of view. Let $\xi(x)$ be the probability that a particle travels at least a distance x without making a collision. The probability of traveling at least a distance $x + dx$ without making a collision is

$$
\xi(x + dx) = \xi(x) - \xi(x)\, dx / \lambda_{tot}(x) \tag{A.16}
$$

and solving for $\xi(x)$ gives

$$\xi(x) = exp\left[-\int_0^x \frac{ds}{\lambda_{tot}(s)}\right] \tag{A.17}$$

which is just Eq. A.15.

The Monte Carlo method of solving Eq. A.14 is to track test flights using Eq. A.17 to determine points of collision. Take a uniform random variable (URV) ξ between 0 and 1 and solve

$$\xi(x) = exp\left[-\int_0^{x(\xi)} \frac{ds}{\lambda_{tot}(s)}\right] \tag{A.18}$$

for the collision point $x(\xi)$. By running a sequence of test flights a distribution of collision points is determined and, knowing the remaining terms in $C(f)$, such as plasma density and temperature and the reaction cross-sections, the distribution function is solved.

In order to solve the integral equation Eq. A.18 for $x(\xi)$, the pseudo-collision algorithm (PCA) is used in DEGAS. Given the initial x_0 and v, let λ_m be the shortest mean free path length in the entire plasma for the test flight. Move the test flight to

$$x_1 = x_0 - ln(\xi)\lambda_{min}v_l \tag{A.19}$$

where ξ is a URV, $0 < \xi < 1$, and $v_1 = v/\|v\|$. Let $\rho = \lambda_{min}/\lambda_{tot}(x_1)$, and test for a collision: Choose a new URV, ξ_1. If $\xi_1 \leq \rho$ then a collision occurs. If $\xi_1 > \rho$ then a pseudo-collision is occurred and the procedure is repeated until a collision occurs.

A.2 Test Flight Weighting

Each test flight is initially given a weight of $\omega = 1$. If a total source of *Jatoms/s* is being modeled with N test flights, each test flight then represents γ = *J/Natoms/s* at its start. As the test flight progresses through a sequence of collisions the weight is reduced to account for attenuation by ionization. This method is called suppressed absorption. ω is multiplied at each collision by the probability of charge exchange, $\rho_{CX} = 1 - \rho_{ion}$. The probability of the ionization ρ_{ion} for atomic hydrogen is represented as follows,

$$\rho_{ion} = \frac{n_e\langle\sigma v\rangle_{ion}^e + n_i\langle\sigma v\rangle_{ion}^i}{n_i\langle\sigma v\rangle_{CX}^e + n_i\langle\sigma v\rangle_{ion}^i + n_e\langle\sigma v\rangle_{ion}^e} \tag{A.20}$$

where $\langle\sigma v\rangle_{ion}^i$ is the rate coefficient for the proton ionization. For example, after the first collision,

a test flight would represent $\rho_{CX}(\gamma\omega)$ *atoms/sec*, with $(1-\rho_{ion})\,(\gamma\omega)$*atoms/sec* having been ionized. This weight attenuation process continues until w is less than some pre-assigned minimum weight ω_{min}. At this point, one reaction between a pure charge exchange or ionization is chosen. In the case of the charge exchange reaction, ω remains unchanged and the flight is continued, while ω is set to be 0 and the flight is ended in the ionization case.

A.3 Scoring

At a collision, a weight of $(1-\rho_{CX})\cdot\omega$ is ionized. The sum

$$\tau_j = \sum(1-\rho_{CX})\omega \tag{A.21}$$

taken over all collisions in plasma zone j of all test flights, represents the ionization rate in zone j, in units of test flight weight. This is converted to S_j *ionizations*/m^3 by multiplying by γ and dividing by the volume vol_j of zone j,

$$S_j = \gamma\tau_j/vol_j \tag{A.22}$$

The charge exchange ion power loss in zone j is equal to

$$\gamma\sum\rho_{CX}\,\omega(\kappa E^+ - E^0)/vol_j \tag{A.23}$$

where the sum is over all collisions in zone j, κ is the charge exchange weight correction coefficient described as follows,

$$\kappa = \frac{\sigma_{CX}\|\mathrm{v}\|}{\langle\sigma\upsilon\rangle_{CX}} \tag{A.24}$$

where σ_{CX} is the charge exchange cross section and $\mathrm{v} = \mathrm{v}_{new} - \mathrm{v}_{old}$ with the incoming test flight velocity v_{old}. A velocity of the neutral after the charge exchange reaction v_{old} is chosen from the Maxwellian distribution of ion velocities. $E0$ is the energy of the incoming neutral and E^+ is the energy of the incoming ion. The power gained by ions due to ionization processes equals

$$\gamma\cdot\sum(1-\rho_{CX})\cdot w\left(E^0 - \rho'_{ion}E^{ion}\right)/vol_j \tag{A.25}$$

where

$$\rho'_{ion} = \frac{n_i \langle \sigma v \rangle^i_{ion}}{n_i \langle \sigma v \rangle^i_{ion} + n_e \langle \sigma v \rangle^e_{ion}} \tag{A.26}$$

is the ion impact ionization probability, and E^{ion} is the energy necessary for ionization. The neutral density n_{0j} in zone j is derived from the relation

$$S_j = n_{0j}(n_{ej} < \sigma_e v > + n_{ij} < \sigma_i v >) \tag{A.27}$$

where the only unknown is n_{0j}. The average energy of neutrals $\bar{E}^0_j$ ionizing in zone j can be computed independently and is given by

$$\bar{E}^0_j = \gamma \cdot \sum (1 - \rho_{CX}) w E^0 / S_j \tag{A.28}$$

where the sum is taken as in Eq. A.21, and $E0$ is the neutral energy at a collision. Equations A.21 and A.28 cannot be used in zones without plasma, because the sums are empty there. In plasma-less regions a fictitious plasma of pseudo-ions Ψ is assumed, whose reaction

$$\Psi + H_0 \rightarrow \Psi + H_0 \tag{A.29}$$

leaves H_0 unchanged in every way. Taking the sum

$$\tau^{\Psi}_j = \sum w \tag{A.30}$$

over all collisions with pseudo-ions in zone j, the neutral density n_{0j} then obeys

$$S^{\Psi}_j = \gamma \tau^{\Psi}_j = \gamma \tau^{\Psi}_j = n_{0j} n_{\psi j} \langle \sigma v \rangle_{\Psi} \tag{A.31}$$

where $n_{\psi j}$ is the pseudo-ion density in zone j and $\langle \sigma v \rangle_{\Psi}$ is the rate coefficient of reaction A.29.

In the DEGAS code, the scorings are made not at each collision but at each pseudo-collision for the improvement of the statistics. For example, the sum in Eq. A.21 is replaced by the sum over all pseudo-collisions in zone j,

$$\tau'_j = \sum \frac{\lambda_{min}}{\lambda} (1 - \rho_{CX})\, \omega \tag{A.32}$$

A.4 Neutral Reflection at Wall

In general, for each projectile/target combination, experiment or computation will give a 5-dimensional differential scattering distribution,

$$P(E,\alpha,v,\theta,\phi)v^2\ dvsin\theta d\theta d\phi \tag{A.33}$$

where E and α are the incident energy and polar angle, respectively. v, θ and ϕ are the velocity, polar and azimuthal angles of the reflected particle, respectively. The azimuthal angle is measured from the plane of the incident trajectory. To each incident E and α is associated the 3-dimensional conditional distribution,

$$P_{E,\alpha}(v,\theta,\phi)v^2 dvsin\theta d\theta d\phi \tag{A.34}$$

The parameter of the reflection particle is obtained as follows. First v_0 is chosen from

$$f^1_{E,\alpha}(v) = \iint P_{E,\alpha}(v,\theta,\phi)dvsin\theta d\theta d\phi \tag{A.35}$$

Given v_0 then θ_0 is picked from

$$f^2_{E,\alpha}(\theta) = \iint P_{E,\alpha}(v_0,\theta,\phi)d\phi \tag{A.36}$$

and finally, with v_0 and θ_0 known, ϕ_0 can be chosen from the distribution.

$$f^3_{E,\alpha}(\phi) = P_{E,\alpha}(v_0,\theta_0,\phi) \tag{A.37}$$

where $P_{E,\alpha}$ has been suitably normalized.

A.5 Atomic and Molecular Processes

In the DEGAS code, the following assumptions are included about the plasma-neutral interactions and neutral reflection.

1. The following reactions A.a-A.m show the plasma-neutral interactions included in the DEGAS code.

Charge Exchange:

$$p + H \rightarrow H + p \quad \text{(A. a)}$$
$$H_2^+ + H_2 \rightarrow H_2 + H_2^+ \quad \text{(A. b)}$$
$$p + H_2 \rightarrow H_2^+ + H \quad \text{(A. c)}$$

Electron Impact Ionization:

$$e + H \rightarrow e + H^+ + e \quad \text{(A. d)}$$
$$e + H_2 \rightarrow e + H_2^+ + \text{e} \quad \text{(A. e)}$$

Electron Dissociation:

$$e + H_2 \rightarrow e + H + H \quad \text{(A. f)}$$
$$e + H_2 \rightarrow e + H + H^+ + e \quad \text{(A. g)}$$
$$e + H_2^+ \rightarrow H + H \quad \text{(A. h)}$$
$$e + H_2^+ \rightarrow e + H^+ + e \quad \text{(A. i)}$$
$$e + H_2^+ \rightarrow e + H^+ + H^+ + e \quad \text{(A. j)}$$

Recombination:

$$e + p \rightarrow H \quad \text{(A. k)}$$

Ion Impact Ionization:

$$p + H \rightarrow p + H^+ + e \quad \text{(A. l)}$$
$$p + H_2 \rightarrow p + H_2^+ + e \quad \text{(A. m)}$$

The rate coefficients or cross sections for the reactions are taken from the experimental data and theoretical results which are mainly referred in [59]. CX reaction rates are calculated as a function of the ion temperature, ion density and the energy of neutral particle. The model of electron impact ionization processes of neutral hydrogen includes the effects of multi-step ionization as a function of the plasma density and electron temperature.

2. The effect of the neutral-neutral and neutral-ion elastic scattering is neglected.

3. Neutral hydrogen atoms and molecules sticking to the wall desorb immediately as hydrogen molecules with the energy corresponding to a wall temperature.

Reference

[1] Y. Kamada et al., Nucl. Fusion, 41, No 10 (2001) 1311.

[2] J.W. Hughes et al., Nucl. Fusion, 47 (2007) 1057.

[3] M. Inutake et al, Physi. Rev. Lett. 55 (1985) 939.

[4] T. Tamano, Phys. Plasmas 2 (1995) 2321.

[5] K. Yatsu et al., Nucl. Fusion 39 (1999) 1707.

[6] S. A. Allen et al, Nucl. Fusion 27 (1987) 2149.

[7] K. Hosoi et al., Trans. Fusion Sci. Tech. 59, 1T, (2011) 229-231.

[8] Y. Kubota, Ph. D. Thesis Univ. Tsukuba (2006).

[9] S.L., Milora, et al ., Nucl. Fusion 20 (1980) 1491.

[10] Y. Nakashima et al, J. Nucl. Mater. 196-198 (1992) 493.

[11] D. Reiter et al., J. Nucl. Mater. 196-198 (1992) 1059.

[12] K. Tsuchiya, Ph. D. Thesis Univ. Tsukuba (1994).

[13] S. Kobayashi et al., J. Nucl. Mater. 266-269 (1999) 566.

[14] M. Sakamoto et al., Nucl. Fusion 42 (2002) 165.

[15] L. Yao, in "New Developments in Nuclear Fusion Research" (Nova Sci. Pub, pp. 61-87 2006).

[16] K. Hosoi et al., Plasma Fusion Res. 7, (2012) 2402126.

[17] F. Sano et al. Nucl. Fusion 45 (2005) 1557.

[18] T. Mizuuchi et al., Nucl. Fusion 47 (2007) 395.

[19] N. Nishino et al., J. Nucl. Mater. 337-339 (2005) 1073.

[20] Y. Nakashima et al, J. Nucl. Mater. 241-243 (1997) 1011.

[21] M. Shoji et al., Plasma. Phys. Control. Fusion 43 (2001) 761.

[22] M. Shoji, Ph. D. Thesis Univ. Tsukuba (1995).

[23] S. Kobayashi, Ph. D. Thesis Univ. Tsukuba (2001).

[24] Y. Nakashima et al., J. Plasma Fusion Res. Vol.80, No.10 (2004) 813.

[25] Y. Higashizono et al., Trans. Fusion Technol. 47, No.1T (2005) 297.

[26] Y. Nakashima et al, Rev. Sci. Instrum. 74, (3) (2003) 2115.

[27] M. Yoshikawa et al., Trans. Fusion Technol. 47, No.1T (2005) 339.

[28] D. B. Heifetz et al., J. Comp. Phys. 46 (1982) 309.

[29] D. P. Stotler et al., Phys. Plasmas. 3 (1996) 4084.

[30] K. Muraoka, et al., J. Nucl. Mater. 176-177 (1990) 231.

[31] Y. Nakashima et al., J. Plasma Fus. Res. 6 (2004) 546.

[32] Y. Nakashima, et al., J. Nucl. Mater. 337-339 (2005) 466.

[33] Y. Nakashima et al., J. Plasma Physics vol. 72, part 6 (2006) 1123.

[34] Y. Nakashima, et al., Trans. Fusion Sci. and Technol. 51, No.2T (2007) 82.

[35] Y. Higashizono et al., Trans. Fusion Technol. 51, No.2T (2007) 367.

[36] Y. Higashizono et al., J. Plasma Fus. Res. 2 (2007) S1087.

[37] Y. Higashizono Ph. D. Thesis Univ. Tsukuba (2008).

[38] E. Kawamori, Ph. D. Thesis Univ. Tsukuba (2006).
[39] Y. Kubota, Ph. D. Thesis Univ. Tsukuba (2006).
[40] A. L. Qualls et al., Proc. 13th Symp. Fusion Engineering, No. 2, p.1244.
[41] M. Ichimura et al., Nucl. Fusion 28 (1998) 799
[42] M. Ichimura et al., J. Plasma Fusion Res. SERIES, 3 (2000) 58
[43] T. Imai et al., J. Plasma Fusion Res. 85, (2009) 378-382
[44] M. Yoshikawa et al., Journal of Instrumentation, 7 (2012) C03003.
[45] I. Katsumata: Contrib. Plasma Phys. 36 (1996) S, 73-80
[46] T. Saito et al., Phys. Fluid B 5 (1993) 866.
[47] N. Nishino et al., Plasma Fusion. Res. 1 (2006) 035.
[48] Y. Nakashima et al., J. Nucl. Mater. 363-365 (2007) 616.
[49] H. Kawano et al., J. Plasma Fus. Res. 2 (2007) S1126.
[50] L. C. Johnson and E. Hinnov, J. Quant. Spectrosc. Radiat. Transf. 13 (1973) 333.
[51] T. Fujimoto et al., J. Phys. Soc. Japan 54 (1985) 2905.
[52] K. Sawada et al., Phys. Rev. E 49 (1994) 5565.
[53] Y. Higashizono et al., J. Plasma Fus. Res. 2 (2007) S1087
[54] W. Eckstein and H. Verbeek: Max Plank Institute för Plasmaphisik, IPP-9/32
[55] A. Murakami et al., Plasma Fusion Res. 5 (2010) S1032
[56] A. Murakami et al., J. Plasma Fusion Res. SERIES 9 (2010) 979.
[57] P´egouri´e B. et al., J. Nucl. Mater. 313-316 (2003) 539.
[58] T. Mizuuchi, et al., Contrib. Plasma Phys. 50, No.6-7, (2010) 639 - 645.
[59] A. Murakami et al., Plasma Phys. Control. Fusion 54 (2012) 055006.
[60] R. K. Janev, W. D. Langer, K. Evans Jr., D. E. Post Jr., Elementary Processes in Hydrogen-Helium Plasmas,Springer,Berlin, 1987.

11.5

Study of particle control based on Hα line measurement and Mote-Carlo simulation in the GAMMA 10 tandem mirror Katsuhiro HOSOI February 2014

11

Study of Particle Control Based on Hα Line Measurement and Mote-Carlo Simulation in the GAMMA 10 Tandem Mirror Katsuhiro HOSOI February 2014

10.5

Study of Particle Control Based on Hα Line Measurement and Mote-Carlo Simulation in the GAMMA 10 Tandem Mirror Katsuhiro HOSOI February 2014

10

Study of Particle Control Based on Hα Line Measurement and Mote-Carlo Simulation in the GAMMA 10 Tandem Mirror Katsuhiro HOSOI February 2014